



HAL
open science

Detrital zircon U–Pb–Hf systematics of Ediacaran metasediments from the French Massif Central: Consequences for the crustal evolution of the north Gondwana margin

Simon Couzinié, Oscar Laurent, Cyril Chelle-Michou, Pierre Bouilhol, Jean-Louis Paquette, Abdelmouhcine Gannoun, Jean-François Moyen

► To cite this version:

Simon Couzinié, Oscar Laurent, Cyril Chelle-Michou, Pierre Bouilhol, Jean-Louis Paquette, et al.. Detrital zircon U–Pb–Hf systematics of Ediacaran metasediments from the French Massif Central: Consequences for the crustal evolution of the north Gondwana margin. *Precambrian Research*, 2019, 324, pp.269-284. 10.1016/j.precamres.2019.01.016 . hal-02026217

HAL Id: hal-02026217

<https://uca.hal.science/hal-02026217v1>

Submitted on 22 Oct 2021

HAL is a multi-disciplinary open access archive for the deposit and dissemination of scientific research documents, whether they are published or not. The documents may come from teaching and research institutions in France or abroad, or from public or private research centers.

L'archive ouverte pluridisciplinaire **HAL**, est destinée au dépôt et à la diffusion de documents scientifiques de niveau recherche, publiés ou non, émanant des établissements d'enseignement et de recherche français ou étrangers, des laboratoires publics ou privés.



Distributed under a Creative Commons Attribution - NonCommercial 4.0 International License

1 **Detrital zircon U–Pb–Hf systematics of Ediacaran metasediments from the**
2 **French Massif Central: consequences for the crustal evolution of the**
3 **north Gondwana margin**

4
5 Simon Couzinié^{1,2,3*}, Oscar Laurent⁴, Cyril Chelle-Michou^{4,5}, Pierre Bouilhol³,
6 Jean-Louis Paquette⁶, Abdel-Mouhcine Gannoun⁶, Jean-François Moyen²

7 ¹Université de Lyon, ENSL, UCBL, CNRS, LGL-TPE, F-69007 Lyon, France

8 ²Université de Lyon, Laboratoire Magmas et Volcans, UJM-UCA-CNRS-IRD, F-42023 Saint-
9 Étienne, France

10 ³CRPG, Université de Lorraine, CNRS, UMR7358, 15 rue Notre Dame des Pauvres, F-54501
11 Vandoeuvre Les Nancy, France.

12 ⁴Institute for Geochemistry and Petrology, ETH Zürich, Zurich, Switzerland

13 ⁵School of Earth Sciences, University of Bristol, Wills Memorial Building, Queens Road, Bristol
14 BS8 1RJ, UK

15 ⁶Université Clermont Auvergne, CNRS, IRD, OPGC, Laboratoire Magmas et Volcans, F-63000
16 Clermont-Ferrand, France

17 *corresponding author. simon.couzinie@univ-lorraine.fr

18
19 **Abstract**..... 2
20 **1. Introduction** 3
21 **2. Geological setting** 6
22 **3. Samples and analytical techniques**..... 7
23 **4. Results** 9
24 4.1 Zircon description 9
25 4.2 U–Pb geochronology..... 10
26 4.3 Zircon Hf isotope compositions 11
27 **5. Discussion** 13

28	5.1	Interpretation of U–Pb dates: depositional ages of the sedimentary protoliths and Variscan overprint.....	13
30	5.2	The Ediacaran paleogeography of the EFMC with respect to other Variscan zones 15	
32	5.3	Zircon sources.....	17
33	5.4	Crustal evolution of the EFMC and the North Gondwana margin.....	22
34	6.	Conclusion	24
35		Acknowledgements	26
36		Figures captions	26
37		References	29

38

39 **Abstract**

40

41 Combining U–Pb and Lu–Hf isotopic data of detrital zircon grains has proven a powerful
42 tool to unravel the provenance of sediments and address continental crust evolution. In
43 this study, we explore the origin of thick siliciclastic metasedimentary units from the
44 high-grade internal domains of the Variscan belt of Europe and examine their
45 significance for Neoproterozoic crust formation and evolution along the North
46 Gondwana margin. We present data and U–Pb/Lu–Hf systematics of detrital zircons
47 from five amphibolite-facies metasediments sampled in the eastern French Massif
48 Central, measured in situ by LA–(MC)–ICP–MS. The sedimentary protoliths were
49 deposited in the Ediacaran as evidenced by field relationships and maximum
50 depositional ages ranging between 592.4 ± 5.5 and 556.8 ± 5.1 Ma. All samples
51 contain three main zircon populations in terms of age distribution and Hf isotopes: (i)
52 abundant 0.55–0.65 Ga zircons with considerably scattered $\epsilon\text{Hf}_{(t)}$ from -19 to +14; (ii)
53 varied amounts of 0.65–1.0 Ga zircons showing dominantly positive $\epsilon\text{Hf}_{(t)}$ with the
54 exception of the c. 1.0 Ga zircons; and (iii) ≥ 1.8 Ga zircons (mostly between 1.9–2.1
55 and 2.5–2.8, up to 3.2 Ga) with $\epsilon\text{Hf}_{(t)}$ ranging between +5 and -7. Multidimensional
56 scaling of our U–Pb dataset and a data compilation of Ediacaran to Lower Cambrian

57 (meta)sediments from the North Gondwana margin reveals that the relative proportions
58 of the three age components carry discriminant provenance information. Geological
59 data indicate that the Ediacaran basins of the eastern French Massif Central collected
60 the erosion products of two main source regions: (i) the Neoproterozoic Cadomian
61 magmatic arc; and (ii) the cratonic hinterland, mostly from the Saharan Metacraton and
62 the Arabian-Nubian Shield. Our dataset attests to the reworking of: (i) juvenile
63 Neoproterozoic crust and, (ii) old Paleoproterozoic to Neoproterozoic crustal components,
64 either as part of the detritus or incorporated in Neoproterozoic arc magmas. First-order
65 estimates derived from the isotopic signature of S-type granitic magmas sourced in the
66 Ediacaran metasediments suggest that 60–75% of the detritus would correspond to
67 young Neoproterozoic crust and thus represent net additions to the continental crust
68 volume.

69

70 **Keywords:** North Gondwana margin, French Massif Central, detrital zircons,
71 U–Pb–Hf isotopes, Cadomian orogeny, crustal growth

72

73 **1. Introduction**

74

75 Multi-methods studies based on surface heat flow measurements, seismic profiles and
76 large-scale geochemical surveys concluded that the continental crust has a bulk
77 andesite/diorite composition (e.g. Rudnick and Fountain (1995); Rudnick and Gao
78 (2003); Wedepohl (1995)). Importantly, such composition is not in equilibrium with a
79 mantle peridotite, meaning that new crust generation necessitates the addition of
80 mantle-derived magmas to a pre-existing crustal volume followed by differentiation of
81 the basaltic precursor and foundering of mafic residual materials into the mantle. This
82 hints that the hallmark of crust production is the intrusion of magmas extracted from

83 ultrabasic and young basic igneous sources (Condie and Aster, 2010). However,
84 addressing the rate of crust production based solely on the igneous record has proven
85 ambiguous because magmatic rocks are not always preserved and can experience
86 sedimentary reworking (Iizuka et al., 2005). Consequently, continental sediments and
87 sedimentary rocks have been increasingly used to address the timing, rate and mode
88 of continental crust formation (see review in Dhuime et al. (2017)). In particular, many
89 studies focus on zircon, an accessory mineral of intermediate to felsic igneous rocks
90 characterized by its extreme resilience to mechanical abrasion and low to high-T
91 alteration such that it is very commonly retrieved as detrital grains in sedimentary
92 lithologies. Chronological constraints derived from detrital zircon U–Pb systematics
93 paired with the determination of Lu–Hf isotope compositions of individual grains offer
94 the possibility to gain insights on the age and origin of rocks that have been eroded and
95 thus to genuinely track periods of crust production (Gerdes and Zeh, 2006; Iizuka et al.,
96 2005; Kemp et al., 2006).

97

98 The basement of Western and Central Europe corresponds to a set of crustal blocks
99 amalgamated during the late Paleozoic Variscan *s.l.* collisional orogeny (Franke, 1989;
100 Kroner and Romer, 2013; Matte, 1986). Such blocks are often referred to as
101 ‘Cadmian-type peri-Gondwana terranes’ since they were formerly located at the
102 northern margin of the Gondwana continent by the late Neoproterozoic and were
103 strongly shaped by the Cadomian accretionary orogen featuring a c. 2500 km-long
104 magmatic arc and associated back-arc basin (Garfunkel, 2015; Murphy and Nance,
105 1989; Murphy et al., 2004). Importantly, accretionary orogenic settings are generally
106 retained as the main sites of continental crust production as they encompass
107 voluminous mantle-derived magmatism (Cawood et al., 2009; Reymer and Schubert,
108 1984; Taylor and McLennan, 1985). Yet, within the Cadomian realm, today-exposed
109 mantle-derived volcanic-plutonic associations are scarce, in marked contrast with the

110 well-preserved coeval siliciclastic sedimentary successions deposited at the rear of the
111 arc (Dabard et al., 1996; Denis and Dabard, 1988; Drost et al., 2011; Garfunkel, 2015;
112 Linnemann et al., 2014; Linnemann et al., 2008; Orejana et al., 2015; Pereira et al.,
113 2006; Pereira, 2014; Pereira et al., 2012a; Pereira et al., 2012b; Rabu et al., 1990;
114 Talavera et al., 2015; Talavera et al., 2012). Therefore, such sedimentary rocks would
115 have preserved the best record of the Cadomian orogenic evolution and constitute an
116 ideal target to clarify the extent of Neoproterozoic crust production along the North
117 Gondwana margin.

118

119 Several provenance studies based on heavy minerals or detrital zircon typology and U–
120 Pb(–Hf) signatures have been carried out with the main aim to address the
121 Neoproterozoic paleogeography of the peri-Gondwana terranes, notably their paleo-
122 location along the main Gondwana continent (e.g., (Chelle-Michou et al., 2017; Dabard
123 et al., 1996; Drost et al., 2011; Henderson et al., 2016; Pereira et al., 2012a; Pereira et
124 al., 2012b; Stephan et al., 2018). Investigations so far focused on areas having
125 experienced limited Variscan metamorphic overprint such as the Teplá-Barrandian and
126 Saxo-Thuringian zones of the Bohemian Massif (Drost et al., 2011; Hajná et al., 2017;
127 Linnemann et al., 2007; Linnemann et al., 2014; Linnemann et al., 2017; Žák and
128 Sláma, 2017), the Central Iberian, Ossa-Morena and Cantabrian zones of the Iberian
129 Massif (Díez Fernández et al., 2010; Fernández-Suárez et al., 2014; Naidoo et al.,
130 2017; Orejana et al., 2015; Pereira et al., 2012a; Pereira et al., 2012b; Talavera et al.,
131 2015; Talavera et al., 2012; Teixeira et al., 2011; Zimmermann et al., 2015) and the
132 northern to central Armorican Massif (Ballouard, 2016; Dabard et al., 1996; Denis and
133 Dabard, 1988; Gougeon et al., 2017; Nagy et al., 2002; Rabu et al., 1990), all exposing
134 (very) low to medium-grade Variscan metamorphic units (Fig. 1). In contrast, little is
135 known about the pre-orogenic evolution of the high-grade metamorphic belts building
136 up the Moldanubian zone, regarded as the most internal domain of the Variscan belt

137 (Lardeaux et al., 2014). In this contribution, we report the U–Pb–Hf isotopic
138 compositions of detrital zircon grains from amphibolite-facies metasediments from the
139 eastern French Massif Central measured in situ by LA–(MC)–ICP–MS with the aim to
140 address: (i) the Neoproterozoic paleogeography of this crust segment with respect to
141 adjacent (para)autochthonous Variscan blocks; (ii) the source of the sedimentary
142 supplies; (iii) the relative extent of crust production/reworking during the Cadomian
143 orogeny.

144

145 **2. Geological setting**

146

147 The eastern French Massif Central (EFMC, Fig. 2) exposes two main allochthonous
148 tectonic-metamorphic units (nappes), juxtaposed as a result of collision between
149 Laurussia and Gondwana (Faure et al., 2009b; Ledru et al., 1989). The overlying *Upper*
150 *Gneiss Unit* comprises ortho- and paragneisses having experienced MP–M(H)T
151 amphibolite- to granulite-facies collisional metamorphism at 360–340 Ma (Chelle-
152 Michou et al., 2017). The base of this unit features a bimodal meta-igneous association
153 referred to as the Leptynite-Amphibolite Complex, which hosts petrological relicts of
154 eclogite-facies metamorphism dated at c. 380 Ma in the SW part of the French Massif
155 Central (Lotout et al., 2018), presumably attesting to the closure by subduction of the
156 Galicia-Massif Central oceanic domain. The underlying Lower Gneiss Unit consists of
157 an association of amphibolite-facies micaschists, ortho- and paragneisses with very
158 scarce amphibolites (Ledru et al., 2001). The *Lower Gneiss Unit* experienced
159 significant anatexis at the post-collisional stage (315–300 Ma, e.g. Mougeot et al.
160 (1997)), culminating in the formation of the 120 x 80 km large Velay granite-migmatite
161 dome during orogenic collapse (Ledru et al., 2001; Montel et al., 1992). The Velay
162 dome is overturned to the south onto the low-grade *Parautochthonous Unit*, largely

163 composed of greenschist- to lower amphibolite-facies metasediments. All metamorphic
164 units were intruded by a set of peraluminous to metaluminous granitoids, testifying for
165 protracted magmatic activity between 335 and 300 Ma (Couzinié et al., 2014; Laurent
166 et al., 2017; Villaros et al., 2018).

167

168 Available geochronological data on the protoliths of the metamorphic rocks from the
169 EFMC suggest contrasted pre-Variscan evolutions for each nappe. In the Upper
170 Gneiss Unit, both felsic and mafic meta-igneous lithologies are of Ordovician age (LA–
171 ICP–MS U–Pb and Pb evaporation zircon ages; Chelle-Michou et al. (2017); Feybesse
172 et al. (1995)). Metasediments have not been investigated in the EFMC area but yielded
173 Cambrian maximum depositional ages in the western part of the French Massif Central
174 (LA–ICP–MS U–Pb zircon; Melleton et al. (2010)). In the Lower Gneiss Unit, the
175 protoliths of the Velay Orthogneiss Formation (Fig. 2), an association of augen
176 gneisses and leucogneisses regarded as former S-type granites, were emplaced at c.
177 541 Ma (LA–ICP–MS U–Pb zircon; Couzinié et al. (2017)), i.e. at the Ediacaran–
178 Cambrian transition. Field relationships indicate that these (meta)granites are intrusive
179 within the (meta)sediments of the Lower Gneiss Unit (Ledru et al., 1994) entailing that
180 the latter were deposited in the Precambrian. The abundance of Neoproterozoic
181 inherited zircon cores in the Velay Orthogneiss Formation and other crust-derived
182 Variscan granitoids point to a Neoproterozoic crustal source which likely corresponds
183 to the metasediments (Couzinié et al., 2017; Laurent et al., 2017). This view is
184 consistent with the preliminary results of Chelle-Michou et al. (2017) who obtained 25
185 concordant Neoproterozoic U–Pb zircon dates from a Lower Gneiss Unit paragneiss.
186 Finally, deposition of the thick siliciclastic successions of the Parautochthonous Unit was
187 bracketed by LA–ICP–MS U–Pb zircon dating of interlayered felsic volcanics, all
188 yielding Ordovician ages (Faure et al., 2009a).

189

190 **3. Samples and analytical techniques**

191

192 The sampling strategy was to cover all the metasedimentary units wrapping the Velay
193 migmatite-granite dome, which cores the Lower Gneiss Unit in the EFMC. Five
194 amphibolite-facies metasediments were collected. GPS coordinates and whole-rock
195 major and trace element compositions of the investigated samples are available in
196 Supplementary Table S1. The latter were obtained from the ALS Global firm (details on
197 the procedure and accuracy/reproducibility in Supplementary Material).

198 *PIL-16-01* belongs to a 40 cm-thick metasandstone body interbedded within the
199 aluminous Pilat micaschists (Malavielle et al., 1990), which form a constituent lithology
200 of the Lower Gneiss Unit in the northern part of the Velay Complex (Fig. **2**). This very
201 silicic rock ($\text{SiO}_2 > 87\%$) is dominantly composed of quartz and muscovite with
202 subordinate amounts of feldspar, Fe–Ti oxides and zircon (Fig. **S1a**). The metamorphic
203 evolution has been constrained on surrounding metapelites and features an early stage
204 at 8–10 kbar and $600 \pm 50^\circ\text{C}$ followed by equilibration at 3–5 kbar and $690 \pm 20^\circ\text{C}$
205 (Gardien, 1990).

206 *SEN-16-01* corresponds to a meter-thick quartz-rich layer within the Senouire
207 micaschists, a typical metasedimentary unit of the western flank of the Velay Complex
208 (Ledru et al., 1994). The specimen is mostly composed of quartz and biotite with minor
209 amounts of muscovite, garnet, plagioclase, Fe–Ti oxides and zircon (Fig. **S1b**). Peak
210 metamorphic conditions for this unit have been estimated at $630 \pm 20^\circ\text{C}$ and 5–6 kbar
211 (Mintrone, 2016).

212 *CHA-16-02* was sampled from a 20 cm-thick meta-arkose layer closely associated with
213 amphibolite-facies micaschists from the southwestern part of the Velay Complex
214 (Briand et al., 1993). The rock is clearly a meta-arkose because of its moderate
215 $\text{SiO}_2/\text{Al}_2\text{O}_3$ and $\text{Fe}_2\text{O}_3/\text{K}_2\text{O}$ ratios (lower than 6 and 0.7 respectively; Herron (1988)) and

216 the high modal proportion of feldspar which, together with quartz, constitutes most of
217 the rock. Other minerals include garnet, muscovite, Fe–Ti oxides and zircon (Fig. **S1c**).
218 *TN46* is a coarse-grained, anatectic paragneiss collected in the eastern part of the
219 dome in the Tournon area (Fig. **2**) and already described in Chelle-Michou et al.
220 (2017). The sample is dominantly composed of quartz, plagioclase, alkali-feldspar and
221 biotite together with scarce sillimanite.

222 *PdB-16-01* is an anatectic paragneiss taken from the migmatite exposure of Pont de-
223 Bayzan in the southern part of the dome (described in Montel et al. (1992)). Only the
224 melanocratic part of the sample, presumably corresponding to residuum in the sense of
225 Sawyer (2008), was selected for zircon analysis. The mineral assemblage consists of
226 quartz, plagioclase, alkali-feldspar and biotite with accessory zircon, monazite and
227 apatite (Fig. **S1d**). According to Montel et al. (1992), partial melting took place at 650–
228 720°C and 3–4.5 kbar.

229

230 Zircon grains were separated from crushed rock samples using standard techniques at
231 Saint-Etienne University, described in Couzinié et al. (2016). More than 100 and up to
232 300 randomly selected grains were cast in epoxy resin and polished down to an
233 equatorial grain section. Cathodoluminescence imaging was performed at (i) the
234 Laboratoire Magmas et Volcans in Clermont-Ferrand, France using a Jeol JSM-5910
235 and (ii) the University of Bristol, UK using a Hitachi S-3500N SEM. Zircon U–Pb
236 isotopic analyses were carried out at ETH Zürich, Switzerland by laser ablation–
237 inductively coupled plasma–sector field–mass spectrometry (LA–ICP–SF–MS) using a
238 RESOLUTION (ASI, Australia) 193 nm ArF excimer laser system coupled to an Element
239 XR (Thermo Scientific, Germany) sector-field mass spectrometer. Lu–Hf isotope
240 measurements were performed at the Laboratoire Magmas et Volcans using a Thermo
241 Scientific Neptune Plus multi-collector ICP–MS coupled to the same RESOLUTION 193
242 nm laser excimer system as described above. Comprehensive descriptions of the

243 methodologies, results of secondary standard and sample measurements for both U-
244 Pb and Lu-Hf isotopes are available as Supplementary Material and Supplementary
245 Table S2 to S5.

246

247 **4. Results**

248

249 4.1 Zircon description

250

251 Zircon grains in the investigated samples are mostly colorless, a few of them being
252 pinkish or yellowish. Their shapes vary from rounded (notably in sample PIL-16-01) to
253 sub-idiomorphic (sample PdB-16-01) with aspect ratios up to 1:3. They range in length
254 from 50 to 160 μm except in sample TN46 from which markedly larger grains were
255 extracted (100 to 300 μm long). The zircon grains are often broken (particularly in
256 samples PIL-16-01 and SEN-16-01). Cathodoluminescence images reveal very diverse
257 internal structures (Fig. **3**). Oscillatory or patchy, broad zoning is common in many
258 grains (see for instance in PdB-16-01, Fig. **3e**). Core-rim relationships are frequent in
259 sample TN46 (e.g. z19, z54 and z84 in Fig. **3d**) but generally lacking in other samples
260 in which only very few crystals show narrow CL-bright or dark rims ($< 10 \mu\text{m}$ -wide, see
261 zircon z83 and z35, Fig. **3a**, or z11, Fig. **3b**). Secondary textures include healed cracks
262 and fractures (e.g. z35, Fig. **3a**) and zones of blurred oscillatory zoning (e.g. z146, Fig.
263 **3c**), which were avoided for U-Pb dating. Otherwise, we did not target any specific
264 population in an attempt to be representative of the overall zircon diversity.

265

266 4.2 U–Pb geochronology

267

268 A total of 745 U–Pb measurements were performed on zircon grains from the five
269 metasediments. Only dates concordant at 95–105% (with concordance defined as
270 $^{206}\text{Pb}/^{238}\text{U}$ date / $^{207}\text{Pb}/^{206}\text{Pb}$ date x 100) will be further considered for interpretation
271 (representing 492 individual analyses). The $^{206}\text{Pb}/^{238}\text{U}$ dates are reported when
272 younger than 1.2 Ga; the $^{207}\text{Pb}/^{206}\text{Pb}$ dates are preferred when older. The preliminary
273 zircon U–Pb–Hf data obtained by Chelle-Michou et al. (2017) on sample TN46 were
274 appended to our new dataset of 67 U–Pb analyses on this sample.

275

276 The detrital zircon date distributions of all samples feature a dominant Ediacaran to late
277 Cryogenian population in the range 550–720 Ma representing between 50 and 75% of
278 the dates and defining a prominent peak at c. 635 Ma (Fig. 4, 5). The remaining
279 analyses are mostly distributed over three main periods: 760–1050 Ma (Tonian to late
280 Stenian), 1.7–2.1 Ga (Paleoproterozoic) and 2.6–3.2 Ga (Neo- to Paleoproterozoic). PIL-
281 16-01 and CHA-16-02 show similar detrital zircon date distributions, with the
282 Ediacaran–Cryogenian and Tonian–Stenian populations representing c. 70% and 14%
283 of the dataset, respectively (Fig. 4a,c and 5a,c). Paleoproterozoic and Archean dates
284 are relatively scarce (< 12% and 6%, respectively). Sample SEN-16-01 differs by a
285 larger proportion of 760–1050 Ma and older-than-1.8 Ga grains (18 and 23%,
286 respectively, Fig. 5b). TN46 paragneiss contains very few Tonian–Stenian grains but
287 an abundant Paleoproterozoic–Neoproterozoic population (36%, Fig. 5d), with dates up to
288 3.27 Ga (spot z7). The zircon U–Pb date spectrum of PdB-16-01 contrasts with that of
289 the other samples because: (i) Tonian–Stenian grains are more abundant than in any
290 other sample, representing 38% of the dataset; and (ii) Paleoproterozoic and
291 Neoproterozoic dates are very scarce (only 4% of the data) (Fig. 5e). CL-dark zircon
292 grains yielding Variscan dates in the range 320–305 Ma were retrieved in sample
293 TN46, as already described and discussed by Chelle-Michou et al. (2017).

294

295 4.3 Zircon Hf isotope compositions

296

297 The zircon grains analyzed for Lu–Hf isotopes were selected as to representatively
298 capture the zircon date distribution for each sample. The results are depicted Fig. 6.

299

300 *PIL-16-01*. Twenty-two 550–665 Ma zircon grains show very diverse $\epsilon\text{Hf}(t)$, from +8.7
301 down to -10.5. One late Tonian grain has a radiogenic $\epsilon\text{Hf}(t)$ of +4.6. Early Tonian to
302 late Stenian zircons also have variable Hf isotope signatures with 3 grains displaying
303 $\epsilon\text{Hf}(t)$ of -11.9, +1.6 and +10.8 ϵ -units. Five Paleoproterozoic zircons range between -
304 7.4 and +4.0 ϵ -units. Three Neoproterozoic grains are chondritic to suprachondritic, with
305 $\epsilon\text{Hf}(t)$ ranging from -0.4 up to +4.1.

306

307 *CHA-16-02*. The Hf isotope signature of 32 Ediacaran–Cryogenian zircons (565–720
308 Ma) is highly scattered with $\epsilon\text{Hf}(t)$ ranging from -16.9 up to +12.7. Tonian–Stenian
309 ($n=6$) and Paleoproterozoic ($n=1$) grains display chondritic to supra-chondritic $\epsilon\text{Hf}(t)$
310 (between +0.5 and +12.3). Three Neoproterozoic zircons are nearly chondritic with $\epsilon\text{Hf}(t)$
311 ranging between -2.0 and +1.2.

312

313 *PdB-16-01*. Zircons with U–Pb dates in the range 590–980 Ma have dominantly very
314 radiogenic Hf isotope signatures: 84% of the data yield $\epsilon\text{Hf}(t)$ higher than +4.4, and
315 47% show values overlapping with those for the Depleted Mantle (up to +13.7). Beside
316 this, 8% are nearly chondritic (between -1.8 and 1.2) and the remaining 8%
317 subchondritic (between -12.1 and -18.7). Paleoproterozoic zircon grains show slightly
318 non-radiogenic signatures ($\epsilon\text{Hf}(t)$ of c. -2). Two Neoproterozoic grains yielded sub and
319 suprachondritic values of -5.6 and +2.6.

320

321 *TN46*. Results for this sample were obtained by Chelle-Michou et al. (2017) and are
322 briefly summarized hereafter. Zircon grains with U–Pb dates in the range 560–650 Ma
323 show very scattered $\epsilon\text{Hf}(t)$ ranging from +5.6 down to -19.1. Two early Cryogenian–
324 Tonian grains have identical and very radiogenic Hf isotope signatures of +7.5. Four
325 Paleoproterozoic grains display unradiogenic signatures with $\epsilon\text{Hf}(t)$ between -3.0 and -
326 15.5. Archean zircons have chondritic to negative $\epsilon\text{Hf}(t)$ between +0.2 and -4.2.

327

328 *General pattern*. The $\epsilon\text{Hf}(t)$ measured on Paleoproterozoic and Archean zircon are
329 highly scattered from sub to suprachondritic values. Detrital zircons crystallized at the
330 Tonian–Stenian boundary have even more diverse signatures with $\epsilon\text{Hf}(t)$ ranging from -
331 19 up to +11 (in the field of composition expected for the Depleted Mantle reservoir). A
332 large majority of early Cryogenian–Tonian zircons (mostly represented by sample Pdb-
333 16-01) have very radiogenic Hf isotope signatures. Ediacaran–late Cryogenian zircon
334 grains are typified by their highly variable $\epsilon\text{Hf}(t)$, from -19.1 up to +12.2.

335

336 **5. Discussion**

337

338 5.1 Interpretation of U–Pb dates: depositional ages of the sedimentary
339 protoliths and Variscan overprint

340

341 Field relationships indicate that (meta)granites from the Velay Orthogneiss Formation
342 are intrusive within the (meta)sediments of the Lower Gneiss Unit (Ledru et al., 1994).
343 The oldest emplacement age determined for the metagranite samples (545.9 ± 4.3 Ma,
344 leucogneiss MM09; Couzinié et al. (2017)) entails that the minimum depositional age of
345 the sediments is Ediacaran. One single spot (#116) from a zircon grain in sample PIL-
346 16-01 yielded a concordant date that is significantly younger than this inferred minimum

347 deposition age, i.e. 526 ± 5 Ma (Fig. 5a). This zircon grain is therefore regarded as an
348 outlier, which possibly experienced Pb loss. Excluding this grain, all dates are older
349 than c. 545 Ma, so that the youngest zircon population in each sample can be
350 reasonably considered as representative of the maximum deposition age. The latter
351 has been estimated via the following procedure. First, the youngest (and older than c.
352 545 Ma) concordant analysis is identified. A Concordia date is then calculated out of it
353 and the closest older analysis. If the MSWD of concordance and equivalence lies in the
354 range of acceptable values (which depends on the number of analyses, see Spencer et
355 al. (2016)), the dates are statistically indistinguishable. The next older analysis is then
356 added to this pool and a new Concordia date calculated. This procedure is repeated
357 until the MSWD falls out of the acceptable range. Maximum depositional ages range
358 from 592.4 ± 5.5 Ma for sample PdB-16-01 down to 556.8 ± 5.1 Ma for PIL-16-01 (Fig.
359 **4**). Samples SEN-16-01, CHA-16-02 and TN46 show intermediate (and identical)
360 maximum depositional ages of 567.7 ± 6.0 , 568.3 ± 4.9 and 566.3 ± 6.2 Ma,
361 respectively.

362

363 Among the five samples, zircon grains yielding Variscan dates were only retrieved from
364 the anatectic paragneiss TN46 for which a Concordia date of 307.3 ± 5.1 Ma
365 ($MSWD_{C+E} = 1.3$) can be calculated out of three equivalent analyses. Following Chelle-
366 Michou et al. (2017), we interpret this date as reflecting the age of partial melting in this
367 part of the Lower Gneiss Unit. Apart from this sample, our dataset is indicative of scant
368 zircon neo- and/or re-crystallization during Variscan metamorphism as Variscan grains
369 are commonly lacking and overgrowth zones are scarce and narrow. Even though the
370 investigated samples equilibrated at amphibolite-facies conditions, reaching partial
371 melting for two of them, the Variscan imprint on the zircon budget remained very
372 limited, and the zircon age distribution clearly records the pre-Variscan evolution of the
373 protoliths.

374

375 5.2 The Ediacaran paleogeography of the EFMC with respect to other
376 Variscan zones

377 In this section, we aim to identify the provenance of the crustal segment that
378 constitutes the high-grade Lower Gneiss Unit of the EFMC by addressing its
379 paleographic relationships with adjacent, non-metamorphic to low-grade Variscan
380 zones. For this purpose, we compiled the results of 19 detrital zircon studies conducted
381 on Ediacaran to Lower Cambrian (meta)sediments from several Variscan zones (Fig.
382 1) and compared the detrital zircon date distributions to those observed in the EFMC.
383 Comparison was quantified by non-metric multidimensional scaling (MDS) (Borg and
384 Groenen, 2005), a statistical technique recently expanded to the field of provenance
385 studies (Vermeesch, 2013). A total of 54 samples were retained based on the cut-off
386 criterion “at least 51 zircon dates concordant at 95–105%” (with concordance defined
387 as $^{206}\text{Pb}/^{238}\text{U}$ date / $^{207}\text{Pb}/^{206}\text{Pb}$ date x 100), which corresponds to the number of grains
388 needed to be certain at 95% that no fraction representing more than 10% of the actual
389 population has been missed (Vermeesch, 2004). Calculations were computed using
390 the open-source R language (Ihaka and Gentleman, 1996) and the package
391 `provenance` (Vermeesch et al., 2016). As the U–Pb data were obtained from several
392 laboratories, with different analytical methods (LA–ICP–MS, SHRIMP) and associated
393 analytical uncertainties, we used the Sircombe-Hazelton L2-norm (Sircombe and
394 Hazelton, 2004) as dissimilarity measure, as recommended by Vermeesch (2018). The
395 resultant MDS “map” is displayed figure 7a.

396

397 Two major parameters control the variability of the U-Pb date distributions in
398 Ediacaran–Lower Cambrian (meta)sediments from the North Gondwana margin:(i) the
399 proportions of ≥ 1.8 Ga zircons (captured by Dim_1); and (ii) the relative importance of

400 the Ediacaran–late Cryogenian (<0.65 Ga) vs. early Cryogenian–Tonian (0.65–1.0 Ga)
401 zircons in the Neoproterozoic population (Dim₂) (Fig. **7b**). Specifically, the higher the
402 value of Dim₁, the greater the proportions of zircons with Paleoproterozoic and older U–
403 Pb dates. Samples with elevated Dim₂ (such as NE13–1) feature a unimodal Ediacaran
404 date peak, whereas detrital zircon dates from low-Dim₂ samples (e.g. PNC1) are more
405 evenly distributed throughout the Ediacaran–Tonian time interval.

406

407 In the Dim1-Dim2 projection, Ediacaran–Lower Cambrian (meta)sediments from each
408 Variscan zone plot within restricted domains (Fig. **7a**). Importantly, samples from the
409 Lower Gneiss Unit of the EFMC display a large variety of detrital zircon date
410 distributions among this North Gondwana scheme. Paragneiss sample TN46 contains
411 little 0.65–1.0 Ga zircon but a significant proportion of older-than-1.8 Ga grains, a
412 pattern similar to those observed in Ediacaran–Lower Cambrian (meta)sediments from
413 the Bohemian Massif. In contrast, samples PdB16-01 and SEN16-01 are akin to
414 (meta)sediments of the Central Iberian Zone, being particularly characterized by the
415 abundance of 0.65–1.0 Ga zircons. PIL16-01 and CHA16-01 plot in an intermediate
416 position with respect to these two endmembers. Altogether, the samples from the
417 EFMC Lower Gneiss Unit straddle the fields outlined by all the other Variscan zones
418 and no perfect match exists with any of them. Consequently, if the EFMC
419 metasediments were originally part of a single sedimentary basin (as suggested by
420 geological evidence), such basin can be regarded as a singular Ediacaran
421 paleogeographic domain. The marked variations of the detrital zircon date distributions
422 between individual samples of the EFMC can be interpreted in two different ways. A
423 first possibility would be to consider that they reflect lateral and local variations of the
424 sediment supply within the Ediacaran basin. Alternatively, they could indicate an
425 evolution of the sources of the detritus throughout the Ediacaran (of which timescales
426 cannot be captured within the precision of the LA-ICP-MS dating and the lack of

427 stratigraphic relationship between the samples), i.e. changes in paleo-streams and/or
428 tectonic setting delivering eroded materials from at least two different areas.

429

430 5.3 Zircon sources

431

432 Multi-methods studies (encompassing geochemistry, petrography, sedimentology,
433 geochronology) have demonstrated that Ediacaran sediments deposited along the
434 northern margin of Gondwana were of mixed origin. A fraction of the detritus originated
435 from the erosion of the Cadomian magmatic arc and the rest was supplied by a
436 composite inland Gondwana-derived source (Abbo et al., 2015; Dabard et al., 1996;
437 Denis and Dabard, 1988; Drost et al., 2011; Linnemann et al., 2014; Linnemann et al.,
438 2008; Orejana et al., 2015; Pereira et al., 2012a; Pereira et al., 2012b; Rabu et al.,
439 1990). However, there is no consensus on the relative extent of proximal vs. distal
440 supplies and the actual nature of the hinterland source. Several authors propose that
441 each peri-Gondwana terrane received distal detritus from specific domains of
442 Gondwana such as the Amazonian Craton, West African Craton, Saharan Metacraton
443 and Arabian Nubian Shield (Dörr et al., 2015; Henderson et al., 2016; Stephan et al.,
444 2018). Yet, the case of the Lower Gneiss Unit of the EFMC is still disputed as
445 Henderson et al. (2016) and Stephan et al. (2018) argue for a West African Craton
446 supply while Chelle-Michou et al. (2017) retain a Saharan Metacraton provenance. In
447 addition, none of those authors discuss the extent to which the erosion of the
448 Cadomian magmatic arc contributed to the observed detrital zircon age distributions in
449 the EFMC. In this section, we therefore (i) review the geological and isotopic
450 characteristics of the Cadomian arc and address its potential implication as a proximal
451 source for the Ediacaran EFMC sediments; and (ii) further discuss the nature of the
452 distal source based on the newly obtained, extensive dataset.

453

454 The largest and best preserved exposures of the Cadomian magmatic arc crop out in
455 the northern Armorican Massif (France and British Channel Islands, see Ballèvre et al.
456 (2001); Brown (1995); Chantraine et al. (2001); Strachan et al. (1996)). Even though
457 the exposed rocks may not correspond to those eroded at Ediacaran times, they can
458 still provide constraints on the nature, age pattern and isotopic signature of the
459 proximal detritus. In this crust segment, igneous rocks include: (i) late Cryogenian to
460 early Ediacaran (660–560 Ma) calc-alkaline suites comprising basic, intermediate and
461 acid components with radiogenic to unradiogenic Nd–Hf isotope signatures, taken as
462 evidence for arc–back-arc magmatism; (ii) late Ediacaran migmatites and peraluminous
463 granitoids (the Mancellian batholith, 560–540 Ma), proposed to have been generated
464 during back-arc basin inversion and resulting arc–continent collision. Scarce
465 Paleoproterozoic and Tonian crustal rocks (Icartian and Pentevrian gneisses,
466 respectively) are also documented. Figure **8a,b** presents a compilation of intrusion
467 ages available for igneous rocks from the northern Armorican Massif and obtained via
468 different geochronological methods (zircon and monazite U–Pb dating by LA–ICP–MS,
469 SIMS, EPMA and TIMS on single grains or multi-grain fractions for the latter technique,
470 whole-rock Rb–Sr). The observed age populations (540–750, c. 1800 and 2000–2200
471 Ma) are partly consistent with the spread of U–Pb dates in the detrital zircon record of
472 the EFMC. Importantly, the two subpeaks at 585 and 615 Ma observed in the latter
473 perfectly match the igneous dataset. Magmatic rocks emplaced in the time period 625–
474 750 Ma are present, but scarce in the Armorican Massif. This may reflect either a
475 sampling bias or the fact that Cadomian subduction and related magmatism were not
476 yet active at that time (as suggested by the Cadomian geological record elsewhere in
477 Europe, e.g. Garfunkel (2015)). The $\epsilon_{\text{Hf}}(t)$ of various Cadomian intrusions are depicted
478 in figure **8c** (from Hf isotope studies or recalculated from Nd isotopes based on the
479 relation $\epsilon_{\text{Hf}}(t) = 1.36 \epsilon_{\text{Nd}}(t) + 3$ determined by Vervoort et al. (1999)). Magmas

480 emplaced in the time period 750–620 Ma have supra-chondritic, DM-like Hf isotope
481 signatures. A clear shift towards less radiogenic source compositions occurred in the
482 Ediacaran, as magmas younger than 620 Ma show a broad range of inferred $\epsilon\text{Hf}(t)$
483 from +5 down to sub-chondritic values of -11. In general, a large spread of radiogenic
484 isotope signatures at a given time period is interpreted to reflect the contamination of
485 juvenile magmas by old crustal remnants via AFC-type processes and/or magma or
486 source mixing as observed in many arcs built up on ancient continental crust (Bolhar et
487 al., 2008; Kelemen et al., 2003; Kemp et al., 2006).

488 Such a pattern is similar to that observed in the detrital zircon record of metasediments
489 from the Lower Gneiss Unit, yet slightly offset in time (to younger ages in the case of
490 Armorican rocks, Fig. **8c**). The case of Tonian–Stenian, Paleoproterozoic and Archean
491 zircon grains is more problematic as there are no rocks of such ages or appropriate
492 isotopic signatures in the Armorican Massif. There, Paleoproterozoic granitoids have
493 suprachondritic, DM-like, $\epsilon\text{Hf}(t)$ which are more elevated than those observed in detrital
494 zircons from the EFMC Ediacaran (meta)sediments (Fig. **8c**). Altogether, these
495 observations indicate that, our present state of knowledge, erosion of the Cadomian
496 arc *alone* unsatisfactorily explains the U–Pb–Hf systematics of the EFMC detritus thus
497 calling for the existence of an additional zircon source i.e. the main Gondwana land
498 (Drost et al., 2011; Linnemann et al., 2014; Linnemann et al., 2008; Orejana et al.,
499 2015; Pereira et al., 2012a; Pereira et al., 2012b).

500

501 By the mid-Ediacaran, the northern part of Gondwana had just been assembled and
502 stabilized following the late Cryogenian–Ediacaran Pan African orogenies (see
503 Garfunkel (2015)). The Gondwana crust (Fig. **9**) typically comprises cratonic domains
504 of Paleoproterozoic to Archean age (West African, Congo, Chad, Al Kufrah, Murzuq
505 cratons, see Liégeois et al. (2013)) and several Pan African mobile belts (Anti-Atlas,
506 Trans-Sahara and Oubanguides belts, East African orogen, Saharan Metacraton).

507 Most Pan African belts are composed of reworked cratonic crust (“metacraton”) and
508 remnants of 850–620 Ma-old subduction zone-type magmatic activity (oceanic arc
509 accretion, continental arc systems) predating voluminous syn- to post-collisional
510 magmatism at 620–570 Ma (Caby, 2003; Liégeois et al., 2003; Triantafyllou et al.,
511 2016). Remobilization of ancient Paleoproterozoic to Archean crust is notably
512 fingerprinted by the highly variable $\epsilon\text{Nd}(t)$ displayed by Ediacaran to late Cryogenian
513 igneous rocks from the Trans-Sahara (Liégeois et al., 1998; Liégeois et al., 2003), Anti-
514 Atlas (Errami et al., 2009), and Oubanguides (Toteu et al., 2001) belts. Only the
515 Arabian-Nubian-Shield crust segment can be regarded as a juvenile Neoproterozoic
516 terrane (Stern, 2002). In the following, we attempt to identify the areas that would have
517 delivered distal detritus to the EFMC Ediacaran basins based on the igneous record of
518 northern Gondwana.

519

520 Clearly, a supply from western African terranes must be disregarded because: (i)
521 Paleoproterozoic rocks from the West African Craton have suprachondritic Hf isotope
522 signatures whereas zircon grains of that age in the EFMC show a broad range of $\epsilon\text{Hf}(t)$
523 (Fig. 6); (ii) Tonian rocks from the Trans-Sahara belt show subchondritic Nd isotope
524 compositions (Liégeois et al., 1998) while the signature of Tonian EFMC grains points
525 to a radiogenic source (Fig. 6). An East African provenance encompassing erosion
526 products from the Saharan Metacraton and the Arabian Nubian Shield is preferred for
527 several reasons. First, early Cryogenian to Tonian igneous rocks in these areas are
528 typified by suprachondritic Nd–Hf isotope signatures, matching the detrital record of the
529 EFMC (Küster and Liégeois, 2001; Küster et al., 2008; Morag et al., 2011; Morag et al.,
530 2012; Stern et al., 2010). Second, the sole fragments of late Stenian crust in north
531 Gondwana have been described in the northern part of the Arabian Nubian Shield
532 (Be'eri-Shlevin et al., 2012) and could represent the source of EFMC late Stenian
533 zircon grains. Third, the zircon U–Pb–Hf systematics of recent detritus carried along by

534 the Nile river strikingly resemble the Ediacaran detrital zircon record of the EFMC (Fig.
535 **8d**) with two Neoproterozoic vertical arrays (550–650 and 950–1050 Ma), early
536 Cryogenian to Tonian radiogenic detritus (650–950 Ma) and adequate (largely sub-
537 chondritic) range of $\epsilon_{\text{Hf}}(t)$ for the Paleoproterozoic and Archean grains (Be'eri-Shlevin
538 et al., 2014; Iizuka et al., 2013). As the river largely drains the eastern part of the
539 Sahara Metacraton and the Arabian Nubian Shield, we propose that the distal detritus
540 that fed the EFMC Ediacaran basin was sourced from both of these crustal domains.

541

542 Constraining the relative proportions of proximal vs. distal supplies within the EFMC
543 basin has proven ambiguous. The 0.65–1.0 and older-than-1.8 Ga zircon populations
544 most likely originate from erosion of the Sahara Metacraton/Arabian Nubian Shield but
545 the case of 0.55–0.65 Ga grains is controversial as both the Cadomian arc and the Pan
546 African mobile belts represent adequate suppliers. Nonetheless in this case and as
547 shown above, the Cadomian arc can only contribute to the 0.58–0.61 Ga zircons since
548 magmatic activity in the Armorican Massif peaked at that time (Fig. **8b**). Finally,
549 variations in the proportions of 0.55–0.65, 0.65–1.0 and older-than-1.8 Ga grains
550 among EFMC metasediments (see section 5.2) possibly reflect temporal changes in
551 the Saharan Metacraton vs. Arabian Nubian Shield distal inputs. When Sahara
552 Metacraton supplies were dominant, Ediacaran detritus would have featured abundant
553 older-than-1.8 Ga grains (Meinhold et al., 2011), and led to a zircon U–Pb–Hf pattern
554 akin to sample TN46. In contrast, preferential erosion of the Arabian Nubian Shield
555 would have delivered substantial amounts of 0.65–1.0 Ga grains (Morag et al., 2011;
556 Morag et al., 2012; Stern et al., 2010) and resulted in a pattern similar to that of sample
557 PdB16-01.

558

559 5.4 Crustal evolution of the EFMC and the North Gondwana margin

560

561 The Ediacaran (590–545 Ma) deposition of the Lower Gneiss Unit metasediments
562 stamps the formation of the earliest crustal rocks so far known in the EFMC. The
563 nature (and even existence) of the basement on which the sediments were deposited
564 remains elusive as the EFMC crust segment typically lacks any remnant of pre-
565 Neoproterozoic rocks, neither at surface level (Chelle-Michou et al., 2017; Melleton et
566 al., 2010; Padel et al., 2017; Roques et al., 1995) nor in the lower crustal xenoliths
567 sampled by Cenozoic volcanoes (Féménias et al., 2003; Rossi et al., 2006).
568 Examination of the detrital zircon U–Pb–Hf signature indicates that the Ediacaran
569 basins collected detritus from the adjacent Cadomian magmatic arc and distal sources
570 from eastern Africa (see previous sections). Consequently, the EFMC crust segment
571 grew in the Ediacaran by piling up pre-existing, eroded crustal materials of much
572 contrasted ancestries. From a crust evolution perspective, it is critical to establish the
573 relative proportions of eroded juvenile Neoproterozoic vs. old
574 Paleoproterozoic/Archean materials within the earliest EFMC crust as this would
575 constrain in turn the mechanisms and extent of Neoproterozoic crust production along
576 the North Gondwana margin. Importantly, assessing the amount of young crust based
577 on the proportion of detrital zircon grains showing radiogenic Hf isotope signatures is
578 not relevant because: (i) the low zircon fertility of arc rocks and their tendency to show
579 concordant U–Pb dates (see Dickinson (2008); Moecher and Samson (2006))
580 introduce sampling biases, and; (ii) grains showing unradiogenic Hf isotope signatures
581 but crystallized from hybrid crust–mantle magmas may still encapsulate a juvenile
582 component diluted by the non-stoichiometric incorporation of ancient crustal Hf (Bolhar
583 et al., 2008; Couzinié et al., 2016; Kemp et al., 2006). This is likely the case of
584 unradiogenic Ediacaran–early Cryogenian grains from the EFMC (see section 5.3).

585

586 By contrast, S-type (meta)granites of the Velay Orthogneiss Formation may provide a
587 more reliable probe of the actual amount of Cadomian juvenile detritus within the
588 Ediacaran basins. Following Couzinié et al. (2017), the (meta)granites indeed originate
589 from melting of the Ediacaran metasediments. These rocks show strikingly
590 homogeneous chondritic Hf isotope signatures, which resulted from dissolution of
591 detrital zircon grains and homogenization of their disparate Hf isotope signatures prior
592 to magma emplacement. If true, this model entails that the (meta)granites average the
593 Hf isotope composition of their Ediacaran sedimentary source. Earlier work pointed out
594 three main events of juvenile crust formation (i.e. with DM-like Hf-Nd isotope
595 signatures) in the Gondwanian realm, in the Neoproterozoic (i.e. Cadomian and ANS-
596 like, c. 0.65 Ga-old), Paleoproterozoic (Eburnean, c. 2.1 Ga-old) and Neoproterozoic (c.
597 2.8 Ga-old) (Gerdes and Zeh, 2006; Kemp et al., 2006; Linnemann et al., 2014;
598 Orejana et al., 2015). Therefore, the Hf isotopic composition of the Ediacaran
599 sediments can be viewed as a mixture of those three components in different
600 proportions – in turn sampled by the Velay Orthogneiss Formation (meta)granites.
601 Following this, the chondritic signature of the latter demands that 60–75 % of the
602 Ediacaran detritus in the EFMC corresponds to newly formed (i.e. <100 Ma-old) and
603 isotopically juvenile Neoproterozoic crust (Fig. 10), either formerly part of the Cadomian
604 arc or originating from eastern Africa. This first-order estimate is minimal because
605 newly formed Neoproterozoic crust did not necessarily show a DM-like Hf isotope
606 composition. Several studies indeed documented that the very limited incorporation of
607 recycled crustal materials in the mantle source of arc and post-collisional magmas can
608 shift their Hf isotope composition towards non DM-like values (Nebel et al., 2011;
609 Roberts et al., 2012).

610

611 Interestingly, similar estimates can be obtained from the isotopic signature of several
612 late Ediacaran–early Paleozoic S-type granites from the North Gondwana margin, all

613 presumably derived from melting of Ediacaran sediments. In the Bohemian Massif,
614 magmatic zircons from the c. 540 Ma-old Laubach granite (Linnemann et al., 2014)
615 show a tight range of $\epsilon_{\text{Hf}}(t)$ at 0 ± 2.4 ϵ -units (1 S.D.), identical to that of the Velay
616 Orthogneiss Formation (meta)granites. In the Iberian Massif, the Cambrian–Ordovician
617 volcano-plutonic Ollo de Sapo formation also displays an average $\epsilon_{\text{Hf}}(t)$ of 0 ± 4.1 ϵ -
618 units (1 S.D.) (Montero et al., 2017) whereas in both areas detrital zircons from
619 Ediacaran sediments feature a very wide range of $\epsilon_{\text{Hf}}(t)$, spanning over 30 to 40 ϵ -units
620 (Linnemann et al., 2014; Linnemann et al., 2017; Orejana et al., 2015). Such
621 observations further support the claim that late Ediacaran intra-arc or back-arc basins
622 developed along the North Gondwana margin largely represent newly formed
623 continental crust as they were primarily fed by detritus originating from <100 Ma-old,
624 Neoproterozoic terranes.

625

626 **6. Conclusion**

627

628 In this study, we demonstrate that the Lower Gneiss Unit of the eastern French Massif
629 Central, a portion of the internal (Moldanubian) zone of the late Paleozoic Variscan
630 collisional orogen, encompasses Ediacaran siliciclastic sedimentary successions
631 metamorphosed in the amphibolite-facies at Variscan times. Statistical analysis of
632 detrital zircon U–Pb date distributions reveals that the Lower Gneiss Unit crust
633 segment had a distinct Ediacaran paleogeographic position with respect to adjacent
634 Variscan massifs (Central Iberian Zone, Bohemian Massif, Armorican Massif). Coupled
635 zircon U–Pb–Hf systematics, notably the highly diverse Hf isotope composition
636 displayed by Ediacaran to late Cryogenian individual grains, can be reconciled with
637 Ediacaran detritus being collected from the adjacent Cadomian continental arc plus
638 additional hinterland supplies from eastern African sources (Sahara Metacraton and

639 Arabian Nubian Shield). A dominant proportion of the detritus (60–75% according to
640 our first-order, minimal estimates) represents fragments of Neoproterozoic crustal
641 materials extracted from the mantle shortly prior to erosion, transport and
642 sedimentation in the Ediacaran basins of the EFMC. Therefore, even though
643 substantial amounts of genuine mantle-derived Neoproterozoic igneous rocks
644 experienced sedimentary reworking and were not preserved, their erosion products
645 were collected in an (attenuated) crustal environment (the intra-arc or back-arc basins)
646 and became de facto long-term additions to the continental crust volume. Importantly,
647 the existence of concomitant sedimentary inputs from distal cratonic sources and the
648 incorporation of old crustal materials in continental arc magmas resulted in this newly
649 formed crust being intrinsically heterogeneous from an Hf isotope perspective. Several
650 studies argued that a scatter in the zircon $\epsilon\text{Hf}(t)$ at a given time period, as observed in
651 the Ediacaran–Cryogenian record of the North Gondwana margin, reflects the
652 dominance of crust reworking processes (Dhuime et al., 2017; Kemp et al., 2006;
653 Vervoort and Kemp, 2016). In contrast, this work shows that such a situation may just
654 as well reflect voluminous new crust production.

655

656 **Acknowledgements**

657

658 C. Guilbaud made the thin sections; J.-M. Hénot assisted during SEM imaging; M.
659 Ballèvre provided the file of Fig. 1; M. Mintrone contributed to Fig. 2; A. Laurent, A.
660 Vezinet, A. Villaros, V. Gardien and G. Mahéo participated to stimulating discussions;
661 C. Storey, U. Linnemann and an anonymous reviewer substantially improved the
662 manuscript; may they all be thanked.

663

664 **Figures captions**

665

666 Figure 1: Sketch map of the crustal blocks involved in the Variscan orogeny, adapted
667 from Ballevre et al. (2014). Yellow stars highlight the location of detrital zircon studies
668 performed on Ediacaran–Lower Cambrian (meta)sediments and considered section
669 5.2. Zones: ClZ, Central Iberian; CZ, Cantabrian; GTMZ, Galicia–Trás-os-Montes;
670 OMZ, Ossa-Morena; RHZ, Rheno-Hercynian; SPZ, South-Portuguese; STZ, Saxo-
671 Thuringian; TBZ, Teplá-Barrandian; WALZ, West Asturian–Leonese. VF: Variscan
672 Front. References: 1, Linnemann et al. (2007); 2, Linnemann et al. (2014); 3,
673 Linnemann et al. (2017); 4, Drost et al. (2011); 5, Hajná et al. (2017); 6, Žák and Sláma
674 (2017); 7, Fernández-Suárez et al. (2014); 8, Naidoo et al. (2017) ; 9, Zimmermann et
675 al. (2015); 10, Díez Fernández et al. (2010); 11, Orejana et al. (2015) ; 12, Pereira et
676 al. (2012b) ; 13, Pereira et al. (2012a) ; 14, Talavera et al. (2012); 15, Teixeira et al.
677 (2011); 16, Ballouard (2016) ; 17, Gougeon et al. (2017); 18, Padel et al. (2017); 19,
678 Chelle-Michou et al. (2017).

679

680 Figure 2: Geological map of the Velay dome area showing the location of analyzed
681 metasediments. The extent of Variscan partial melting of the metamorphic lithologies is
682 not shown for sake of clarity. Redrawn after Ledru et al. (2001) and regional geological
683 maps of France at scale 1/50000.

684

685 Figure 3: Representative cathodoluminescence images of zircon grains from Lower
686 Gneiss Unit metasediments. The locations of laser spots (white and yellow circles for
687 U-Pb and Lu-Hf analyses respectively) are indicated along with the spot name (zXX or
688 #YY). The corresponding $^{206}\text{Pb}/^{238}\text{U}$ dates (if <1.2 Ga) or $^{207}\text{Pb}/^{206}\text{Pb}$ dates (if >1.2 Ga)
689 are quoted with 2σ uncertainty, in Ma. All displayed analyses are concordant at >95%.

690 Hf isotope data are reported using the ϵ_{Hf} calculated at the $^{206}\text{Pb}/^{238}\text{U}$ or $^{207}\text{Pb}/^{206}\text{Pb}$
691 date obtained on the same zircon domain, quoted with 2σ uncertainty.

692

693 Figure 4: Tera–Wasserburg diagrams ($^{238}\text{U}/^{206}\text{Pb}$ vs. $^{207}\text{Pb}/^{206}\text{Pb}$) showing
694 Neoproterozoic zircon data for the Lower Gneiss Unit metasediments. Error
695 ellipses/ages are quoted at 2σ level of uncertainty. Colored ellipses are those included
696 in Concordia age calculations. Dotted ellipses for TN46 refer to data from Chelle-
697 Michou et al. (2017).

698

699 Figure 5: Zircon U–Pb date distribution of investigated metasediments from the Lower
700 Gneiss Unit represented as Kernel Density Estimates (KDE). Only 95–105%
701 concordant $^{206}\text{Pb}/^{238}\text{U}$ (for dates < 1.2 Ga) and $^{207}\text{Pb}/^{206}\text{Pb}$ dates (for dates > 1.2 Ga)
702 were considered. Circles below the x-axis are the central value of individual data
703 points. Plotted with the DensityPlotter program of Vermeesch (2012) using an adaptive
704 bandwidth.

705

706 Figure 6: Combined U-Pb and Lu-Hf isotopic data for zircons from Ediacaran
707 metasediments, constituent rocks of the Lower Gneiss Unit in the Eastern French
708 Massif Central. The data for sample TN46 are from Chelle-Michou et al. (2017). The
709 $\epsilon_{\text{Hf}}(t)$ range for the Depleted Mantle reservoir is bracketed by the models of Naeraa et
710 al. (2012) and Griffin et al. (2002). The dotted arrow represents the isotopic evolution of
711 continental crust (calculated using an average crustal $^{176}\text{Lu}/^{177}\text{Hf}$ ratio of 0.0113).

712

713 Figure 7: (a) Non-metric multi-dimensional scaling plot of the Ediacaran–Lower
714 Cambrian (meta)sedimentary dataset comprising 54 samples from several zones of the
715 Variscan belt. Samples from the Ossa-Morena zone ($n=2$) are not depicted for sake of
716 clarity. See section 5.3 for details on the calculations. (b) Same plot on which the zircon

717 U–Pb date distributions of four selected samples from the literature are displayed with
718 the aim to highlight the end-member zircon populations.

719

720 Figure 8: (a–b) Available intrusion ages for igneous rocks older than 550 Ma in the
721 northern Armorican Massif compared to the detrital zircon record of the Lower Gneiss
722 Unit in the Eastern French Massif Central, represented as Kernel Density Estimates
723 (KDE). Only 95–105% concordant $^{206}\text{Pb}/^{238}\text{U}$ (for dates < 1.2 Ga) and $^{207}\text{Pb}/^{206}\text{Pb}$ dates
724 (for dates > 1.2 Ga) were considered. Plotted with the DensityPlotter program of
725 Vermeesch (2012) with an adaptive bandwidth. Geochronological data for the
726 Armorican Massif were extracted from the compilation of Thiéblemont et al. (2017)
727 supplemented by results from Inglis et al. (2005); Inglis et al. (2004) and Vidal (1980).
728 (c) Hf isotope signature of igneous rocks from the northern Armorican Massif (from Hf
729 isotope studies or recalculated from Nd isotopes based on the relation $\epsilon\text{Hf}(t) = 1.36$
730 $\epsilon\text{Nd}(t) + 3$ determined by Vervoort et al. (1999)) compared to the detrital zircon record
731 of the EFMC. Data from D'Lemos and Brown (1993); Dabard et al. (1996); Guerrot
732 (1989); Samson and D'Lemos (1998); Samson et al. (2003). (d) U–Pb/Lu–Hf
733 systematics of detrital zircon grains from recent sediments of the Nile River, taken as
734 representative of the eastern part of the Sahara Metacraton and western part of the
735 Arabian Nubian Shield, compared to the EFMC record. Data from Be'eri-Shlevin et al.
736 (2014) and Izuka et al. (2013).

737

738 Figure 9: Geological sketch of the northern part of the Gondwana by the late Ediacaran
739 (c. 560 Ma) delineating the main crustal domains (age and Nd–Hf isotope signature)
740 representing putative zircons sources for the EFMC detritus. Arrows represent the
741 likely sources of the detrital supply that fed the Ediacaran EFMC basin. Inspired from
742 Garfunkel (2015) and references therein.

743

744 Figure 10: Triangular diagram showing $\epsilon\text{Hf}(545 \text{ Ma})$ of a virtual sedimentary material as
745 a function of the relative proportions of juvenile Neoproterozoic (Cadomian and ANS-
746 like), Paleoproterozoic (Eburnean) and Neoproterozoic (Eburnean) and Neoproterozoic (Eburnean) and Neoproterozoic (Eburnean) crust in the latter, assuming
747 identical Hf concentrations in the three end-members. The $\epsilon\text{Hf}(545 \text{ Ma})$ of each
748 component was calculated based on a $^{176}\text{Lu}/^{177}\text{Hf}$ of 0.0113 and extraction from a DM
749 source (considering the average value of the models from Griffin et al. (2002) and
750 Naeraa et al. (2012)). The highlighted value of zero corresponds to the average
751 composition of the Ediacaran metasediments required to explain the zircon Hf isotope
752 signature of the Velay Orthogneiss Formation (and other pre-Variscan granitoids
753 emplaced at the Ediacaran-Cambrian boundary, see text for details).

754

755 **References**

756

- 757 Abbo, A., Avigad, D., Gerdes, A., GÜngör, T., 2015. Cadomian basement and
758 Paleozoic to Triassic siliciclastics of the Taurides (Karacahisar dome, south-central
759 Turkey): Paleogeographic constraints from U–Pb–Hf in zircons. *Lithos* 227, 122-139.
- 760 Ballèvre, M., Le Goff, E., Hébert, R., 2001. The tectonothermal evolution of the
761 Cadomian belt of northern Brittany, France: a Neoproterozoic volcanic arc.
762 *Tectonophysics* 331, 19-43.
- 763 Ballouard, C., 2016. Origine, évolution et exhumation des leucogranites peralumineux
764 de la chaîne hercynienne armoricaine : implication sur la métallogénie de l'uranium.
765 Rennes.
- 766 Be'eri-Shlevin, Y., Eyal, M., Eyal, Y., Whitehouse, M.J., Litvinovsky, B., 2012. The Sa'al
767 volcano-sedimentary complex (Sinai, Egypt): A latest Mesoproterozoic volcanic arc in
768 the northern Arabian Nubian Shield. *Geology* 40, 403-406.

769 Be'eri-Shlevin, Y., Avigad, D., Gerdes, A., Zlatkin, O., 2014. Detrital zircon U–Pb–Hf
770 systematics of Israeli coastal sands: new perspectives on the provenance of Nile
771 sediments. *Journal of the Geological Society* 171, 107-116.

772 Bolhar, R., Weaver, S.D., Whitehouse, M.J., Palin, J.M., Woodhead, J.D., Cole, J.W.,
773 2008. Sources and evolution of arc magmas inferred from coupled O and Hf isotope
774 systematics of plutonic zircons from the Cretaceous Separation Point Suite (New
775 Zealand). *Earth and Planetary Science Letters* 268, 312-324.

776 Borg, I., Groenen, P.J., 2005. *Modern Multidimensional Scaling: Theory and*
777 *Applications*. Springer.

778 Briand, B., Combémourel, R., Couturié, J.-P., Bérard, P., Vautrelle, C., 1993. Notice
779 explicative, Carte géol. France (1/50 000), feuille Le Bleyard (863). BRGM, Orléans.

780 Brown, M., 1995. The late-Precambrian geodynamic evolution of the Armorica segment
781 of the Cadomian belt (France): Distortion of an active continental margin during south-
782 west directed convergence and subduction of a bathymetric high. *Géologie de la*
783 *France* 3, 3-22.

784 Caby, R., 2003. Terrane assembly and geodynamic evolution of central–western
785 Hoggar: a synthesis. *Journal of African Earth Sciences* 37, 133-159.

786 Cawood, P.A., Kröner, A., Collins, W.J., Kusky, T.M., Mooney, W.D., Windley, B.F.,
787 2009. *Accretionary orogens through Earth history*. Geological Society, London, Special
788 Publications 318, 1-36.

789 Chantraine, J., Egal, E., Thiéblemont, D., Le Goff, E., Guerrot, C., Ballèvre, M.,
790 Guennoc, P., 2001. The Cadomian active margin (Northern Armorican Massif, France):
791 a segment of the North Atlantic Panafrican belt. *Tectonophysics* 331, 1-18.

792 Chelle-Michou, C., Laurent, O., Moyen, J.-F., Block, S., Paquette, J.-L., Couzinié, S.,
793 Gardien, V., Vanderhaeghe, O., Villaros, A., Zeh, A., 2017. Pre-Cadomian to late-
794 Variscan odyssey of the eastern Massif Central, France: Formation of the West
795 European crust in a nutshell. *Gondwana Research* 46, 170-190.

796 Condie, K.C., Aster, R.C., 2010. Episodic zircon age spectra of orogenic granitoids:
797 The supercontinent connection and continental growth. *Precambrian Research* 180,
798 227-236.

799 Couzinié, S., Laurent, O., Moyen, J.F., Zeh, A., Bouilhol, P., Villaros, A., 2016. Post-
800 collisional magmatism: Crustal growth not identified by zircon Hf-O isotopes. *Earth and*
801 *Planetary Science Letters* 456, 182-195.

802 Couzinié, S., Laurent, O., Poujol, M., Mintrone, M., Chelle-Michou, C., Moyen, J.-F.,
803 Bouilhol, P., Vezinet, A., Marko, L., 2017. Cadomian S-type granites as basement
804 rocks of the Variscan belt (Massif Central, France): Implications for the crustal
805 evolution of the north Gondwana margin. *Lithos* 286-287, 16-34.

806 Couzinié, S., Moyen, J.F., Villaros, A., Paquette, J.L., Scarrow, J.H., Marignac, C.,
807 2014. Temporal relationships between Mg-K mafic magmatism and catastrophic
808 melting of the Variscan crust in the southern part of Velay Complex (Massif Central,
809 France). *Journal of GEOsciences*, 69-86.

810 D'Lemos, R.S., Brown, M., 1993. Sm–Nd isotope characteristics of late Cadomian
811 granite magmatism in northern France and the Channel Islands. *Geological Magazine*
812 130, 797-804.

813 Dabard, M.P., Loi, A., Peucat, J.J., 1996. Zircon typology combined with Sm-Nd whole-
814 rock isotope analysis to study Brioverian sediments from the Armorican Massif.
815 *Sedimentary Geology* 101, 243-260.

816 Denis, E., Dabard, M.P., 1988. Sandstone petrography and geochemistry of late
817 Proterozoic sediments of the Armorican Massif (France) – A key to basin development
818 during the Cadomian orogeny *Precambrian Research* 42, 189-206.

819 Dhuime, B., Hawkesworth, C.J., Delavault, H., Cawood, P.A., 2017. Continental growth
820 seen through the sedimentary record. *Sedimentary Geology* 357, 16-32.

821 Dickinson, W.R., 2008. Impact of differential zircon fertility of granitoid basement rocks
822 in North America on age populations of detrital zircons and implications for granite
823 petrogenesis. *Earth and Planetary Science Letters* 275, 80-92.

824 Díez Fernández, R., Catalán, J.R.M., Gerdes, A., Abati, J., Arenas, R., Fernández-
825 Suárez, J., 2010. U–Pb ages of detrital zircons from the Basal allochthonous units of
826 NW Iberia: Provenance and paleoposition on the northern margin of Gondwana during
827 the Neoproterozoic and Paleozoic. *Gondwana Research* 18, 385-399.

828 Dörr, W., Zulauf, G., Gerdes, A., Lahaye, Y., Kowalczyk, G., 2015. A hidden Tonian
829 basement in the eastern Mediterranean: Age constraints from U–Pb data of magmatic
830 and detrital zircons of the External Hellenides (Crete and Peloponnesus). *Precambrian
831 Research* 258, 83-108.

832 Drost, K., Gerdes, A., Jeffries, T., Linnemann, U., Storey, C., 2011. Provenance of
833 Neoproterozoic and early Paleozoic siliciclastic rocks of the Teplá-Barrandian unit
834 (Bohemian Massif): Evidence from U–Pb detrital zircon ages. *Gondwana Research* 19,
835 213-231.

836 Errami, E., Bonin, B., Laduron, D., Lasri, L., 2009. Petrology and geodynamic
837 significance of the post-collisional Pan-African magmatism in the Eastern Saghro area
838 (Anti-Atlas, Morocco). *Journal of African Earth Sciences* 55, 105-124.

839 Faure, M., Brouder, P., Thierry, J., Alabouvette, B., Cocherie, A., Bouchot, V., 2009a.
840 Notice explicative, Carte géol. France (1/50 000), feuille Saint-André-de-Valborgne
841 (911). BRGM, Orléans.

842 Faure, M., Lardeaux, J.-M., Ledru, P., 2009b. A review of the pre-Permian geology of
843 the Variscan French Massif Central. *Comptes Rendus Geoscience* 341, 202-213.

844 Féménias, O., Coussaert, N., Bingen, B., Whitehouse, M., Mercier, J.-C.C., Demaiffe,
845 D., 2003. A Permian underplating event in late- to post-orogenic tectonic setting.
846 Evidence from the mafic–ultramafic layered xenoliths from Beaunit (French Massif
847 Central). *Chemical Geology* 199, 293-315.

848 Fernández-Suárez, J., Gutiérrez Alonso, G., Pastor-Galán, D., Hofmann, A.W.,
849 Murphy, J.B., Linnemann, U., 2014. The Ediacaran–Early Cambrian detrital zircon
850 record of NW Iberia: possible sources and paleogeographic constraints. *International*
851 *Journal of Earth Sciences* 103, 1335-1357.

852 Feybesse, J.-L., Lardeaux, J.M., Tegye, M., Peterlongo, J.-M., Kerrien, Y., Lemièrre,
853 B., Maurin, G., Mercier, F., Thiéblemont, D., 1995. Notice explicative, Carte géol.
854 France (1/50 000), feuille Saint-Symphorien-sur-Coise (721). BRGM, Orléans.

855 Franke, W., 1989. Variscan plate tectonics in Central Europe - current ideas and open
856 questions. *Tectonophysics* 169, 221-228.

857 Gardien, V., 1990. Reliques de grenat et de staurotide dans la série métamorphique de
858 basse pression du Mont Pilat (Massif Central français) : témoins d'une évolution
859 tectonométamorphique polyphasée. *Comptes Rendus de l'Académie des Sciences*,
860 Paris 310, 233-240.

861 Garfunkel, Z., 2015. The relations between Gondwana and the adjacent peripheral
862 Cadomian domain—constraints on the origin, history, and paleogeography of the
863 peripheral domain. *Gondwana Research* 28, 1257-1281.

864 Gerdes, A., Zeh, A., 2006. Combined U–Pb and Hf isotope LA-(MC-)ICP-MS analyses
865 of detrital zircons: Comparison with SHRIMP and new constraints for the provenance
866 and age of an Armorican metasediment in Central Germany. *Earth and Planetary*
867 *Science Letters* 249, 47-61.

868 Gougeon, R., Néraudeau, D., Dabard, M.-P., Pierson-Wickmann, A.-C., Polette, F.,
869 Pujol, M., Saint-Martin, J.-P., 2017. Trace Fossils from the Brioverian (Ediacaran–
870 Fortunian) in Brittany (NW France). *Ichnos*, 1-14.

871 Griffin, W.L., Wang, X., Jackson, S.E., Pearson, N.J., O'Reilly, S.Y., Xu, X.-S., Zhou,
872 X., 2002. Zircon chemistry and magma mixing, SE China: In-situ analysis of Hf
873 isotopes, Tonglu and Pingtan igneous complexes. *Lithos* 61, 237-269.

874 Guerrot, C., 1989. Archéen et Protérozoïque dans la chaîne hercynienne ouest-
875 européenne, géochimie isotopique (Sr-Nd-Pb) et géochronologie U-Pb sur zircons.
876 Rennes, p. 206.

877 Hajná, J., Žák, J., Dörr, W., 2017. Time scales and mechanisms of growth of active
878 margins of Gondwana: A model based on detrital zircon ages from the Neoproterozoic
879 to Cambrian Blovice accretionary complex, Bohemian Massif. *Gondwana Research* 42,
880 63-83.

881 Henderson, B.J., Collins, W.J., Murphy, J.B., Gutierrez-Alonso, G., Hand, M., 2016.
882 Gondwanan basement terranes of the Variscan–Appalachian orogen: Baltican,
883 Saharan and West African hafnium isotopic fingerprints in Avalonia, Iberia and the
884 Armorican Terranes. *Tectonophysics* 681, 278-304.

885 Herron, M.M., 1988. Geochemical classification of terrigenous sands and shales from
886 core and log data. *Journal of Sedimentary Petrology* 58, 820-829.

887 Ihaka, R., Gentleman, R., 1996. R: a language for data analysis and graphics. *Journal*
888 *of Computational and Graphical Statistics* 5, 299-344.

889 Iizuka, T., Campbell, I.H., Allen, C.M., Gill, J.B., Maruyama, S., Makoka, F., 2013.
890 Evolution of the African continental crust as recorded by U–Pb, Lu–Hf and O isotopes
891 in detrital zircons from modern rivers. *Geochimica et Cosmochimica Acta* 107, 96-120.

892 Iizuka, T., Hirata, T., Komiya, T., Rino, S., Katayama, I., Motoki, A., Maruyama, S.,
893 2005. U-Pb and Lu-Hf isotope systematics of zircons from the Mississippi River sand:
894 Implications for reworking and growth of continental crust. *Geology* 33, 485.

895 Inglis, J.D., Samson, S.D., D'Lemos, R.S., Miller, B.V., 2005. Timing of Cadomian
896 deformation and magmatism within La Hague, NW France. *Journal of the Geological*
897 *Society, London* 162, 389-400.

898 Inglis, J.D., Samson, S.D., D'Lemos, R.S., Hamilton, M., 2004. U–Pb geochronological
899 constraints on the tectonothermal evolution of the Paleoproterozoic basement of
900 Cadomia, La Hague, NW France. *Precambrian Research* 134, 293-315.

901 Kelemen, P.B., Hanghoj, K., Greene, A.R., 2003. One view of the geochemistry of
902 subduction-related magmatic arcs, with an emphasis on primitive andesite and lower
903 crust, in: Rudnick, R.L. (Ed.), *Treatise on Geochemistry*. Elsevier, pp. 593-659.

904 Kemp, A.I., Hawkesworth, C.J., Paterson, B.A., Kinny, P.D., 2006. Episodic growth of
905 the Gondwana supercontinent from hafnium and oxygen isotopes in zircon. *Nature*
906 439, 580-583.

907 Kroner, U., Romer, R.L., 2013. Two plates — Many subduction zones: The Variscan
908 orogeny reconsidered. *Gondwana Research* 24, 298-329.

909 Küster, D., Liégeois, J.-P., 2001. Sr, Nd isotopes and geochemistry of the Bayuda
910 Desert high-grade metamorphic basement (Sudan): an early Pan-African oceanic
911 convergent margin, not the edge of the East Saharan ghost craton? *Precambrian*
912 *Research* 109, 1-23.

913 Küster, D., Liégeois, J.-P., Matukov, D., Sergeev, S., Lucassen, F., 2008. Zircon
914 geochronology and Sr, Nd, Pb isotope geochemistry of granitoids from Bayuda Desert
915 and Sabaloka (Sudan): Evidence for a Bayudian event (920–900Ma) preceding the
916 Pan-African orogenic cycle (860–590Ma) at the eastern boundary of the Saharan
917 Metacraton. *Precambrian Research* 164, 16-39.

918 Lardeaux, J.M., Schulmann, K., Faure, M., Janoušek, V., Lexa, O., Skrzypek, E., Edel,
919 J.B., tipska, P., 2014. The Moldanubian Zone in the French Massif Central,
920 Vosges/Schwarzwald and Bohemian Massif revisited: differences and similarities.
921 *Geological Society, London, Special Publications* 405, 7-44.

922 Laurent, O., Couzinié, S., Zeh, A., Vanderhaeghe, O., Moyen, J.-F., Villaros, A.,
923 Gardien, V., Chelle-Michou, C., 2017. Protracted, coeval crust and mantle melting
924 during Variscan late-orogenic evolution: U–Pb dating in the eastern French Massif
925 Central. *International Journal of Earth Sciences* 106, 421-451.

926 Ledru, P., Courrioux, G., Dallain, C., Lardeaux, J.M., Montel, J.M., Vanderhaeghe, O.,
927 Vitel, G., 2001. The Velay dome (French Massif Central): melt generation and granite
928 emplacement during orogenic evolution. *Tectonophysics* 342, 207-237.

929 Ledru, P., Lardeaux, J.M., Santallier, D., Autran, A., Quenardel, J.-M., Floc'h, J.-P.,
930 Lerouge, G., Maillet, N., Marchand, J., Ploquin, A., 1989. Where are the nappes in the
931 French Massif central? *Bulletin de la Société Géologique de France* 8, 605-618.

932 Ledru, P., Vitel, G., Marchand, J., Maurin, G., Mercier, F., Turland, M., Etlicher, B.,
933 Dautria, J.M., Liotard, J.M., 1994. Notice explicative, Carte géol. France (1/50 000),
934 feuille Craponne-sur-Arzon (767). BRGM, Orléans.

935 Liégeois, J.-P., Abdelsalam, M.G., Ennih, N., Ouabadi, A., 2013. Metacraton: Nature,
936 genesis and behavior. *Gondwana Research* 23, 220-237.

937 Liégeois, J.-P., Navez, J., Hertogen, J., Black, R., 1998. Contrasting origin of post-
938 collisional high-K calc-alkaline and shoshonitic versus alkaline and peralkaline
939 granitoids. The use of sliding normalization. *Lithos* 45, 1-28.

940 Liégeois, J.P., Latouche, L., Boughrara, M., Navez, J., Guiraud, M., 2003. The LATEA
941 metacraton (Central Hoggar, Tuareg shield, Algeria): behaviour of an old passive
942 margin during the Pan-African orogeny. *Journal of African Earth Sciences* 37, 161-190.

943 Linnemann, U., Gerdes, A., Drost, K., Buschmann, B., 2007. The continuum between
944 Cadomian orogenesis and opening of the Rheic Ocean: Constraints from LA-ICP-MS
945 U-Pb zircon dating and analysis of plate-tectonic setting (Saxo-Thuringian zone,
946 northeastern Bohemian Massif, Germany). *Lithos* 423, 61-96.

947 Linnemann, U., Gerdes, A., Hofmann, M., Marko, L., 2014. The Cadomian Orogen:
948 Neoproterozoic to Early Cambrian crustal growth and orogenic zoning along the
949 periphery of the West African Craton—Constraints from U–Pb zircon ages and Hf
950 isotopes (Schwarzburg Antiform, Germany). *Precambrian Research* 244, 236-278.

951 Linnemann, U., Pereira, F., Jeffries, T.E., Drost, K., Gerdes, A., 2008. The Cadomian
952 Orogeny and the opening of the Rheic Ocean: The diacrony of geotectonic processes

953 constrained by LA-ICP-MS U–Pb zircon dating (Ossa-Morena and Saxo-Thuringian
954 Zones, Iberian and Bohemian Massifs). *Tectonophysics* 461, 21-43.

955 Linnemann, U., Pidal, A.P., Hofmann, M., Drost, K., Quesada, C., Gerdes, A., Marko,
956 L., Gärtner, A., Zieger, J., Ulrich, J., Krause, R., Vickers-Rich, P., Horak, J., 2017. A
957 ~565 Ma old glaciation in the Ediacaran of peri-Gondwanan West Africa. *International*
958 *Journal of Earth Sciences*.

959 Lotout, C., Pitra, P., Poujol, M., Anczkiewicz, R., Van Den Driessche, J., 2018. Timing
960 and duration of Variscan high-pressure metamorphism in the French Massif Central: A
961 multimethod geochronological study from the Najac Massif. *Lithos* 308-309, 381-394.

962 Malavielle, J., Guihot, P., Costa, S., Lardeaux, J.M., Gardien, V., 1990. Collapse of the
963 thickened Variscan crust in the French Massif Central: Mont Pilat extensional shear
964 zone and St. Etienne Late Carboniferous basin. *Tectonophysics* 177, 139-149.

965 Matte, P., 1986. Tectonics and plate tectonics model for the Variscan belt of Europe.
966 *Tectonophysics* 126, 329-374.

967 Meinhold, G., Morton, A.C., Fanning, C.M., Frei, D., Howard, J.P., Phillips, R.J.,
968 Strogon, D., Whitham, A.G., 2011. Evidence from detrital zircons for recycling of
969 Mesoproterozoic and Neoproterozoic crust recorded in Paleozoic and Mesozoic
970 sandstones of southern Libya. *Earth and Planetary Science Letters* 312, 164-175.

971 Melleton, J., Cocherie, A., Faure, M., Rossi, P., 2010. Precambrian protoliths and Early
972 Paleozoic magmatism in the French Massif Central: U–Pb data and the North
973 Gondwana connection in the west European Variscan belt. *Gondwana Research* 17,
974 13-25.

975 Mintrone, M., 2016. Constraining the duration of metamorphic events by modeling of
976 phase equilibrium and diffusion in garnet. Example from the French Massif Central.
977 Clermont-Ferrand, p. 54.

978 Moecher, D., Samson, S., 2006. Differential zircon fertility of source terranes and
979 natural bias in the detrital zircon record: Implications for sedimentary provenance
980 analysis. *Earth and Planetary Science Letters* 247, 252-266.

981 Montel, J.M., Marignac, C., Barbey, P., Pichavant, M., 1992. Thermobarometry and
982 granite genesis: the Hercynian low-P, high-T Velay anatectic dome (French Massif
983 Central). *Journal of Metamorphic Geology* 10, 1-15.

984 Montero, P., Talavera, C., Bea, F., 2017. Geochemical, isotopic, and zircon (U-Pb, O,
985 Hf isotopes) evidence for the magmatic sources of the volcano-plutonic Ollo de Sapo
986 Formation, Central Iberia. *Geologica Acta* 15, 245-260.

987 Morag, N., Avigad, D., Gerdes, A., Belousova, E., Harlavan, Y., 2011. Crustal evolution
988 and recycling in the northern Arabian-Nubian Shield: New perspectives from zircon Lu–
989 Hf and U–Pb systematics. *Precambrian Research* 186, 101-116.

990 Morag, N., Avigad, D., Gerdes, A., Harlavan, Y., 2012. 1000–580 Ma crustal evolution
991 in the northern Arabian-Nubian Shield revealed by U–Pb–Hf of detrital zircons from late
992 Neoproterozoic sediments (Elat area, Israel). *Precambrian Research* 208-211, 197-
993 212.

994 Mougeot, R., Respaut, J.P., Ledru, P., Marignac, C., 1997. U-Pb chronology on
995 accessory minerals of the Velay anatectic dome (French Massif Central). *European*
996 *Journal of Mineralogy* 9, 141-156.

997 Murphy, J.B., Nance, R.D., 1989. Model for the evolution of the Avalonian-Cadomian
998 belt. *Geology* 17, 735.

999 Murphy, J.B., Pisarevsky, S.A., Nance, R.D., Keppie, J.D., 2004. Neoproterozoic-Early
1000 Paleozoic evolution of peri-Gondwanan terranes: implications for Laurentia-Gondwana
1001 connections. *International Journal of Earth Sciences* 93, 659-682.

1002 Naeraa, T., Schersten, A., Rosing, M.T., Kemp, A.I., Hoffmann, J.E., Kokfelt, T.F.,
1003 Whitehouse, M.J., 2012. Hafnium isotope evidence for a transition in the dynamics of
1004 continental growth 3.2 Gyr ago. *Nature* 485, 627-630.

1005 Nagy, E.A., Samson, S.D., D'Lemos, R.S., 2002. U–Pb geochronological constraints
1006 on the timing of Brioverian sedimentation and regional deformation in the St. Brieuc
1007 region of the Neoproterozoic Cadomian orogen, northern France. *Precambrian*
1008 *Research* 116, 1-17.

1009 Naidoo, T., Zimmermann, U., Vervoort, J., Tait, J., 2017. Evidence of early Archean
1010 crust in northwest Gondwana, from U–Pb and Hf isotope analysis of detrital zircon, in
1011 Ediacaran supracrustal rocks of northern Spain. *International Journal of Earth*
1012 *Sciences*.

1013 Nebel, O., Vroon, P.Z., van Westrenen, W., Iizuka, T., Davies, G.R., 2011. The effect of
1014 sediment recycling in subduction zones on the Hf isotope character of new arc crust,
1015 Banda arc, Indonesia. *Earth and Planetary Science Letters* 303, 240-250.

1016 Orejana, D., Merino Martínez, E., Villaseca, C., Andersen, T., 2015. Ediacaran–
1017 Cambrian paleogeography and geodynamic setting of the Central Iberian Zone:
1018 Constraints from coupled U–Pb–Hf isotopes of detrital zircons. *Precambrian Research*
1019 261, 234-251.

1020 Padel, M., Álvaro, J.J., Clausen, S., Guillot, F., Poujol, M., Chichorro, M., Monceret, É.,
1021 Pereira, M.F., Vizcaíno, D., 2017. U–Pb laser ablation ICP-MS zircon dating across the
1022 Ediacaran–Cambrian transition of the Montagne Noire, southern France. *Comptes*
1023 *Rendus Geoscience*.

1024 Pereira, M., Chichorro, M., Linnemann, U., Eguluz, L., Silva, J., 2006. Inherited arc
1025 signature in Ediacaran and Early Cambrian basins of the Ossa-Morena Zone (Iberian
1026 Massif, Portugal): Paleogeographic link with European and North African Cadomian
1027 correlatives. *Precambrian Research* 144, 297-315.

1028 Pereira, M.F., 2014. Potential sources of Ediacaran strata of Iberia: a review.
1029 *Geodinamica Acta* 27, 1-14.

1030 Pereira, M.F., Linnemann, U., Hofmann, M., Chichorro, M., Solá, A.R., Medina, J.,
1031 Silva, J.B., 2012a. The provenance of Late Ediacaran and Early Ordovician siliciclastic

1032 rocks in the Southwest Central Iberian Zone: Constraints from detrital zircon data on
1033 northern Gondwana margin evolution during the late Neoproterozoic. *Precambrian*
1034 *Research* 192-195, 166-189.

1035 Pereira, M.F., Solá, A.R., Chichorro, M., Lopes, L., Gerdes, A., Silva, J.B., 2012b.
1036 North-Gondwana assembly, break-up and paleogeography: U–Pb isotope evidence
1037 from detrital and igneous zircons of Ediacaran and Cambrian rocks of SW Iberia.
1038 *Gondwana Research* 22, 866-881.

1039 Rabu, D., Chantraine, J., Chauvel, J.J., Denis, E., Balé, P., Bardy, P., 1990. The
1040 Brioverian (Upper Proterozoic) and the Cadomian orogeny in the Armorican Massif, in:
1041 D'Lemos, R.S., Strachan, R.A., Topley, C.G. (Eds.), *The Cadomian Orogeny*.
1042 *Geological Society Special Publication*, pp. 81-94.

1043 Reymer, A., Schubert, G., 1984. Phanerozoic addition rates to the continental crust and
1044 crustal growth. *Tectonics* 3, 63-77.

1045 Roberts, N.M.W., Slagstad, T., Parrish, R.R., Norry, M.J., Marker, M., Horstwood,
1046 M.S.A., 2012. Sedimentary recycling in arc magmas: geochemical and U–Pb–Hf–O
1047 constraints on the Mesoproterozoic Suldal Arc, SW Norway. *Contributions to*
1048 *Mineralogy and Petrology* 165, 507-523.

1049 Roques, M., Pin, C., Duthou, J.-L., 1995. Prehercynian basement and Hercynian
1050 collision in the french Massif Central. *Comptes Rendus de l'Académie des Sciences*,
1051 *Paris* 320, 817-821.

1052 Rossi, P., Cocherie, A., Fanning, C.M., Deloule, É., 2006. Variscan to eo-Alpine events
1053 recorded in European lower-crust zircons sampled from the French Massif Central and
1054 Corsica, France. *Lithos* 87, 235-260.

1055 Rudnick, R.L., Fountain, D.M., 1995. Nature and composition of the continental crust: a
1056 lower crustal perspective. *Reviews of Geophysics* 33, 267-309.

1057 Rudnick, R.L., Gao, S., 2003. Composition of the continental crust, in: Rudnick, R.L.
1058 (Ed.), *The Crust*. Elsevier-Pergamon, Oxford, pp. 1-64.

1059 Samson, S.D., D'Lemos, R.S., 1998. U–Pb geochronology and Sm–Nd isotopic
1060 composition of Proterozoic gneisses, Channel Islands, UK. *Journal of the Geological*
1061 *Society, London* 155, 609-618.

1062 Samson, S.D., D'Lemos, R.S., Blichert-Toft, J., Vervoort, J., 2003. U–Pb
1063 geochronology and Hf–Nd isotope compositions of the oldest Neoproterozoic crust
1064 within the Cadomian orogen: new evidence for a unique juvenile terrane. *Earth and*
1065 *Planetary Science Letters* 208, 165-180.

1066 Sawyer, E.W., 2008. *Atlas of Migmatites*. NRC Research Press.

1067 Sircombe, K.N., Hazelton, M.L., 2004. Comparison of detrital zircon age distributions
1068 by kernel functional estimation. *Sedimentary Geology* 171, 91-111.

1069 Spencer, C.J., Kirkland, C.L., Taylor, R.J.M., 2016. Strategies towards statistically
1070 robust interpretations of in situ U–Pb zircon geochronology. *Geoscience Frontiers* 7,
1071 581-589.

1072 Stephan, T., Kroner, U.W.E., Romer, R.L., 2018. The pre-orogenic detrital zircon
1073 record of the Peri-Gondwanan crust. *Geological Magazine*, 1-27.

1074 Stern, R.A., Ali, K.A., Liégeois, J.P., Johnson, P.R., Kozdroj, W., Kattan, F.H., 2010.
1075 Distribution and significance of pre-Neoproterozoic zircons in juvenile Neoproterozoic
1076 igneous rocks of the Arabian Nubian Shield. *American Journal of Science* 310, 791-
1077 811.

1078 Stern, R.J., 2002. Crustal evolution in the East African Orogen: a neodymium isotopic
1079 perspective. *Journal of African Earth Sciences* 34, 109-117.

1080 Strachan, R.A., D'Lemos, R.S., Dallmeyer, R.D., 1996. Neoproterozoic evolution of an
1081 active plate margin: North Armorican Massif, France, in: Nance, R.D., Thompson, M.D.
1082 (Eds.), *Avalonian and Related Peri-Gondwanan Terranes of the Circum–North Atlantic*.
1083 *Geological Society of America Special Paper*, Boulder, Colorado, pp. 319-332.

1084 Talavera, C., Martínez Poyatos, D., González Lodeiro, F., 2015. SHRIMP U–Pb
1085 geochronological constraints on the timing of the intra-Alcudian (Cadomian) angular

1086 unconformity in the Central Iberian Zone (Iberian Massif, Spain). *International Journal*
1087 *of Earth Sciences* 104, 1739-1757.

1088 Talavera, C., Montero, P., Martínez Poyatos, D., Williams, I.S., 2012. Ediacaran to
1089 Lower Ordovician age for rocks ascribed to the Schist–Graywacke Complex (Iberian
1090 Massif, Spain): Evidence from detrital zircon SHRIMP U–Pb geochronology.
1091 *Gondwana Research* 22, 928-942.

1092 Taylor, S.R., McLennan, S.M., 1985. *The Continental Crust: its Composition and*
1093 *Evolution*. Blackwell, Oxford.

1094 Teixeira, R.J.S., Neiva, A.M.R., Silva, P.B., Gomes, M.E.P., Andersen, T., Ramos,
1095 J.M.F., 2011. Combined U–Pb geochronology and Lu–Hf isotope systematics by LAM–
1096 ICPMS of zircons from granites and metasedimentary rocks of Carrazeda de Ansiães
1097 and Sabugal areas, Portugal, to constrain granite sources. *Lithos* 125, 321-334.

1098 Thiéblemont, D., Guerrot, C., Simien, F., Zammit, C., 2017. Une compilation des âges
1099 radiochronologiques publiés antérieurement à 2016 sur le Massif armoricain. Inventaire
1100 et mise en forme des données, perspectives pour des acquisitions futures. *Géologie de*
1101 *la France* 1, 27-46.

1102 Toteu, S.F., Van Schmus, W.R., Penaye, J., Michard, A., 2001. New U–Pb and Sm–Nd
1103 data from north-central Cameroon and its bearing on the pre-Pan African history of
1104 central Africa. *Precambrian Research* 108, 45-73.

1105 Triantafyllou, A., Berger, J., Baele, J.-M., Diot, H., Ennih, N., Plissart, G., Monnier, C.,
1106 Watlet, A., Bruguier, O., Spagna, P., Vandycke, S., 2016. The Tachakoucht–Iriri–Tourtit
1107 arc complex (Moroccan Anti-Atlas): Neoproterozoic records of polyphased subduction-
1108 accretion dynamics during the Pan-African orogeny. *Journal of Geodynamics* 96, 81-
1109 103.

1110 Vermeesch, P., 2004. How many grains are needed for a provenance study? *Earth and*
1111 *Planetary Science Letters* 224, 441-451.

1112 Vermeesch, P., 2012. On the visualisation of detrital age distributions. *Chemical*
1113 *Geology* 312-313, 190-194.

1114 Vermeesch, P., 2013. Multi-sample comparison of detrital age distributions. *Chemical*
1115 *Geology* 341, 140-146.

1116 Vermeesch, P., 2018. Dissimilarity measures in detrital geochronology. *Earth-Science*
1117 *Reviews* 178, 310-321.

1118 Vermeesch, P., Resentini, A., Garzanti, E., 2016. An R package for statistical
1119 provenance analysis. *Sedimentary Geology* 336, 14-25.

1120 Vervoort, J.D., Kemp, A.I.S., 2016. Clarifying the zircon Hf isotope record of crust–
1121 mantle evolution. *Chemical Geology* 425, 65-75.

1122 Vervoort, J.D., Patchett, P.J., Blichert-Toft, J., Albarède, F., 1999. Relationships
1123 between Lu–Hf and Sm–Nd isotopic systems in the global sedimentary system. *Earth*
1124 *and Planetary Science Letters* 168, 79-99.

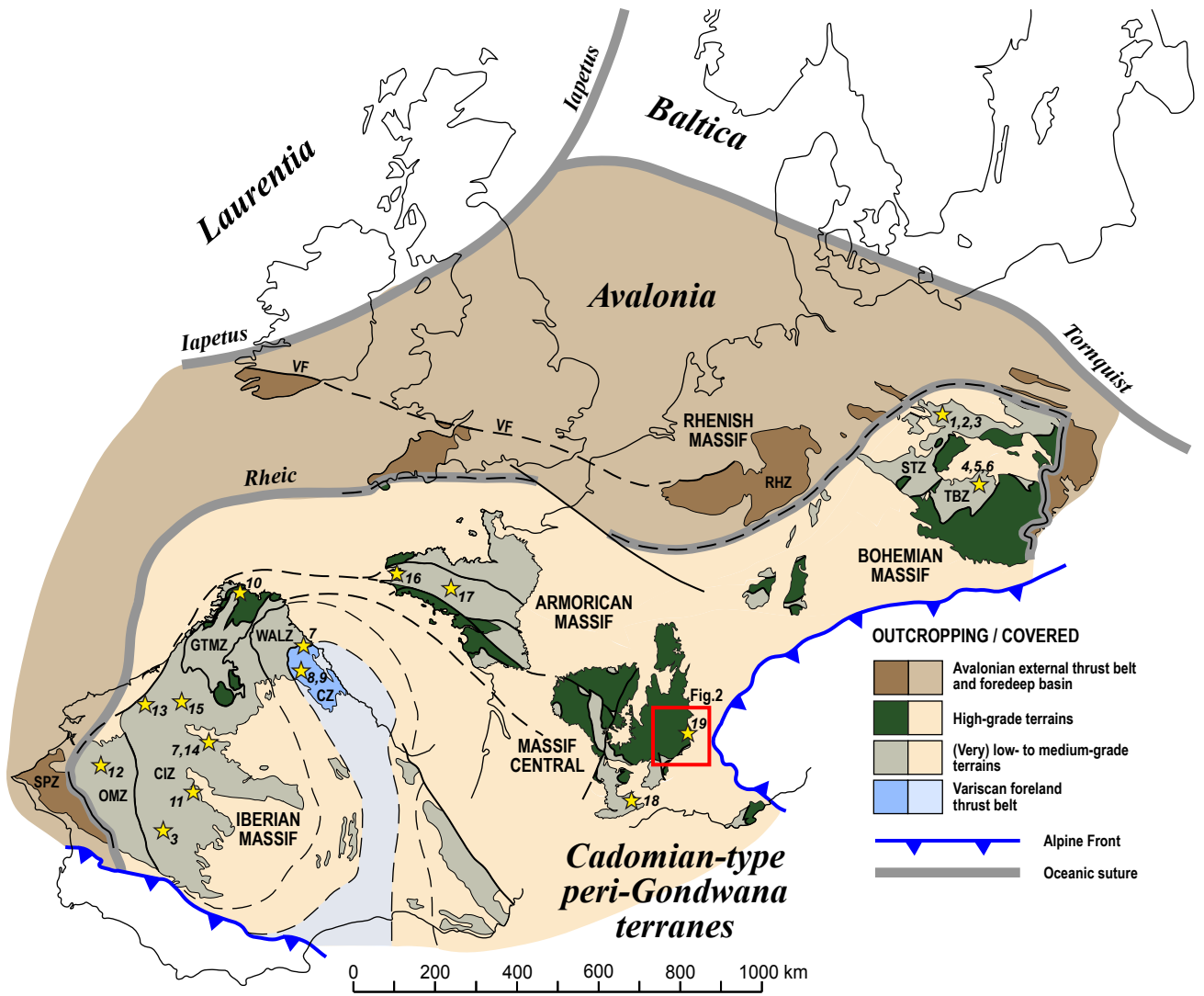
1125 Vidal, P., 1980. L'évolution polyorogénique du Massif armoricain. Apport de la
1126 géochronologie et de la géochimie isotopique du strontium.

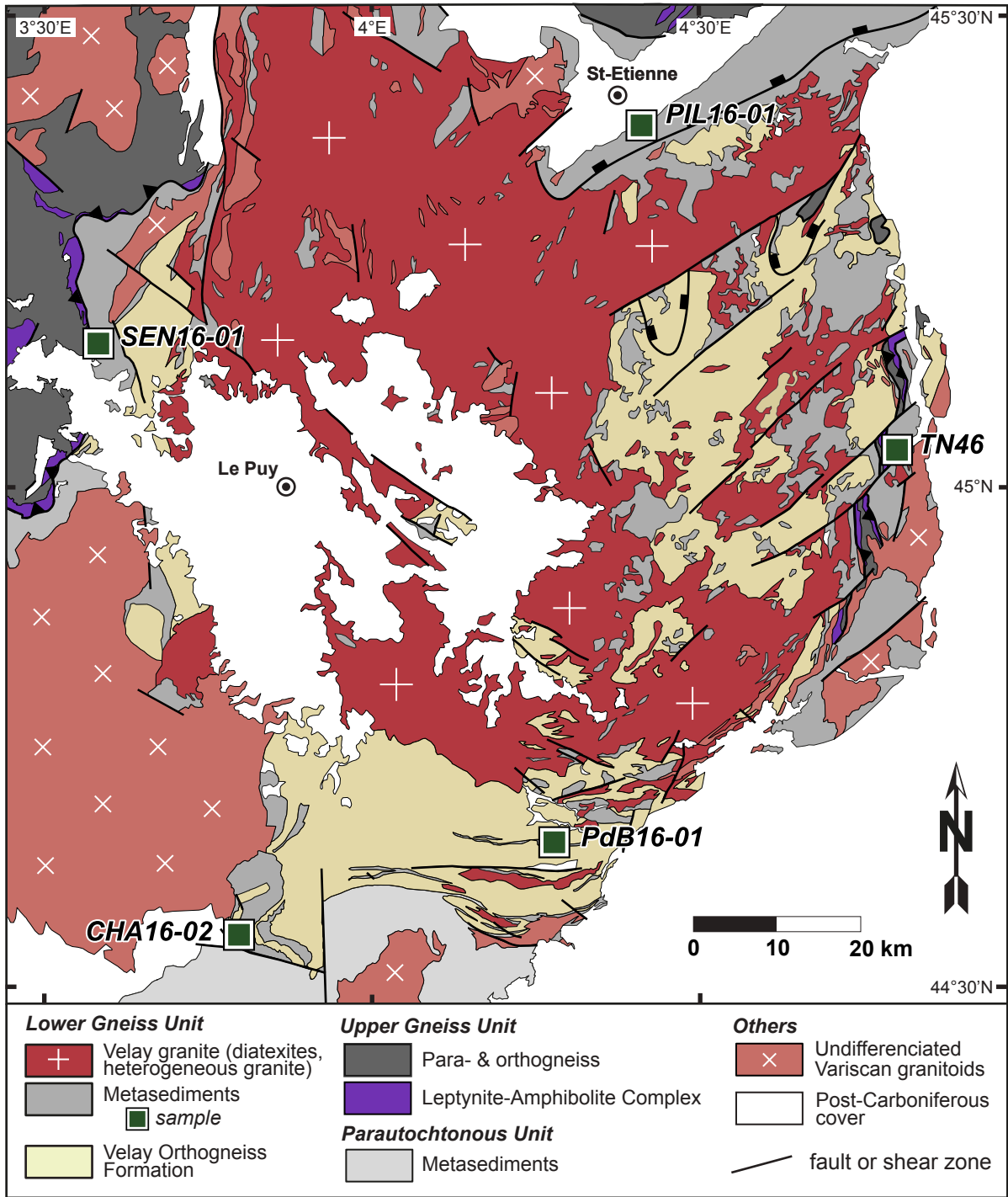
1127 Villaros, A., Laurent, O., Couzinié, S., Moyen, J.F., Mintrone, M., 2018. Plutons and
1128 domes: the consequences of anatectic magma extraction—example from the
1129 southeastern French Massif Central. *International Journal of Earth Sciences*.

1130 Wedepohl, K.H., 1995. The composition of the continental crust. *Geochimica et*
1131 *Cosmochimica Acta* 59, 1217-1232.

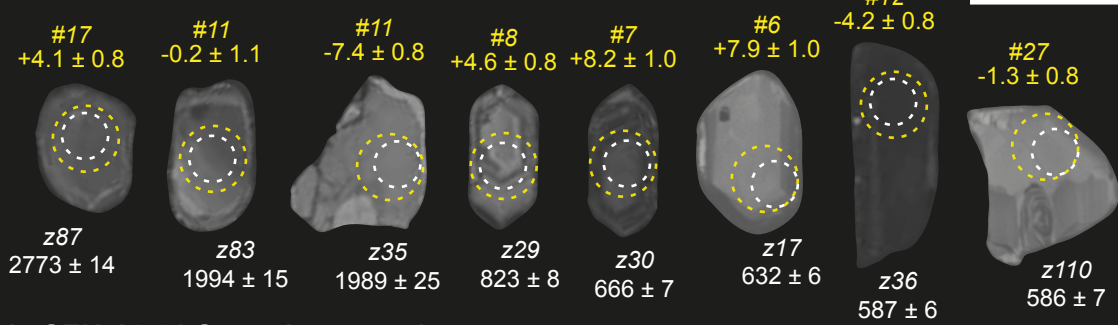
1132 Žák, J., Sláma, J., 2017. How far did the Cadomian 'terrane' travel from Gondwana
1133 during early Palaeozoic? A critical reappraisal based on detrital zircon geochronology.
1134 *International Geology Review*, 1-20.

1135 Zimmermann, U., Andersen, T., Madland, M.V., Larsen, I.S., 2015. The role of U-Pb
1136 ages of detrital zircons in sedimentology—An alarming case study for the impact of
1137 sampling for provenance interpretation. *Sedimentary Geology* 320, 38-50.

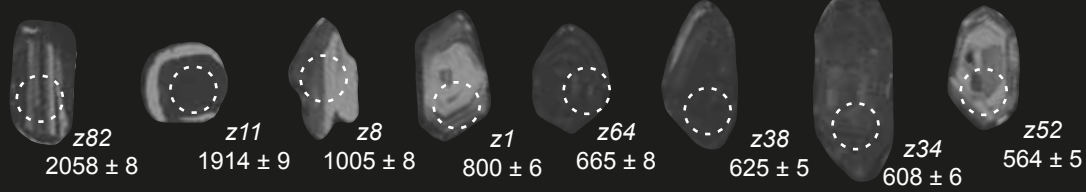




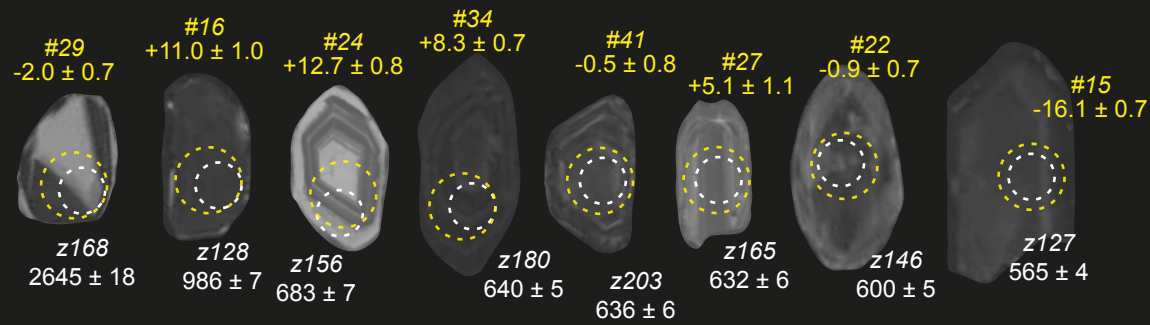
a. PIL-16-01 Pilat quartzite



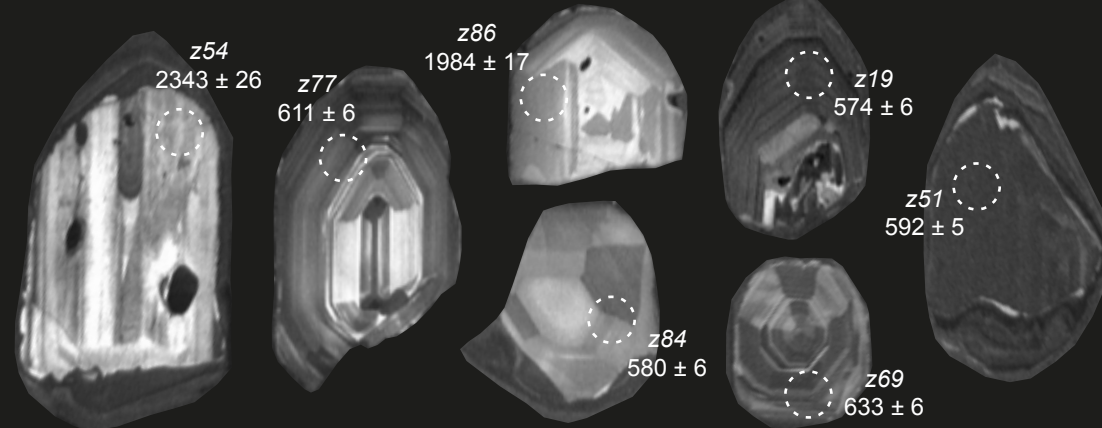
b. SEN-16-01 Senouire quartzite



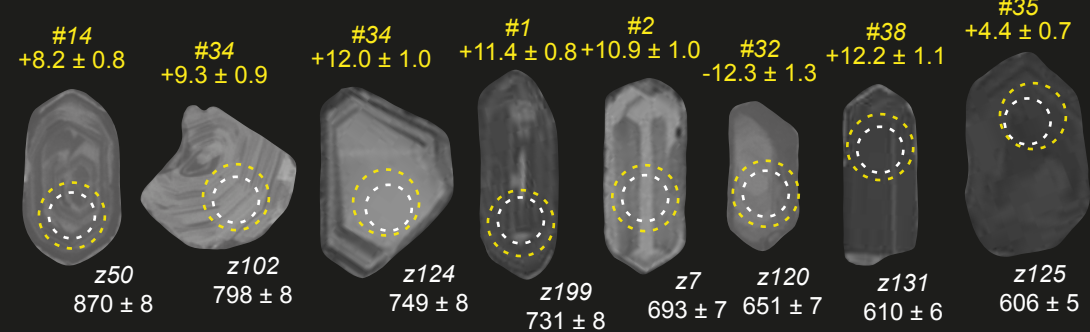
c. CHA-16-02 Cévennes meta-arkose



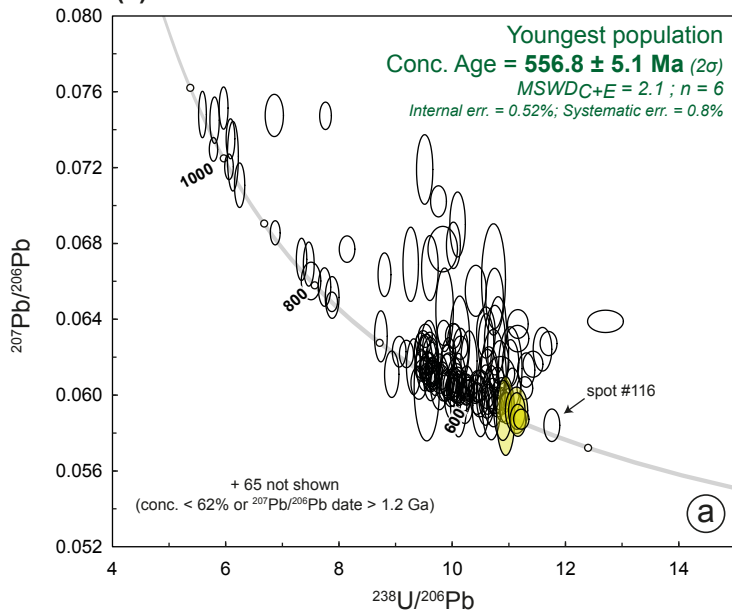
d. TN46 Tounon paragneiss



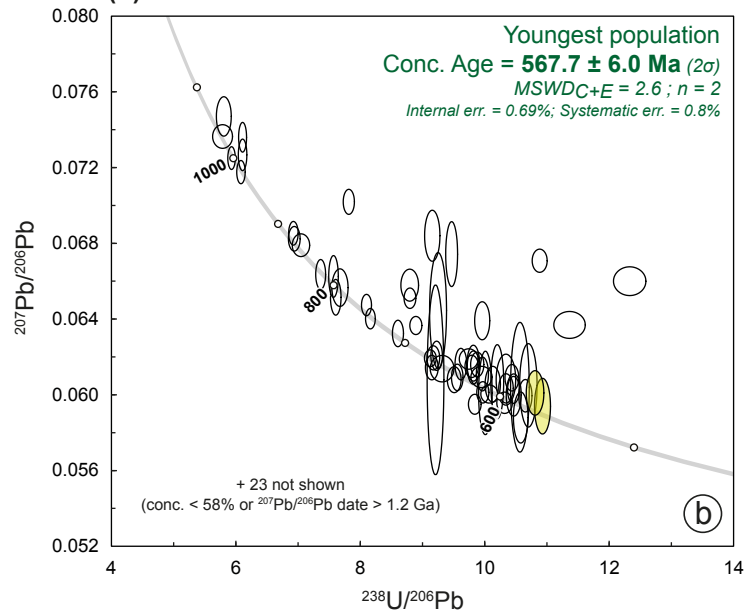
e. PdB-16-01 Pont-de-Bayzan paragneiss



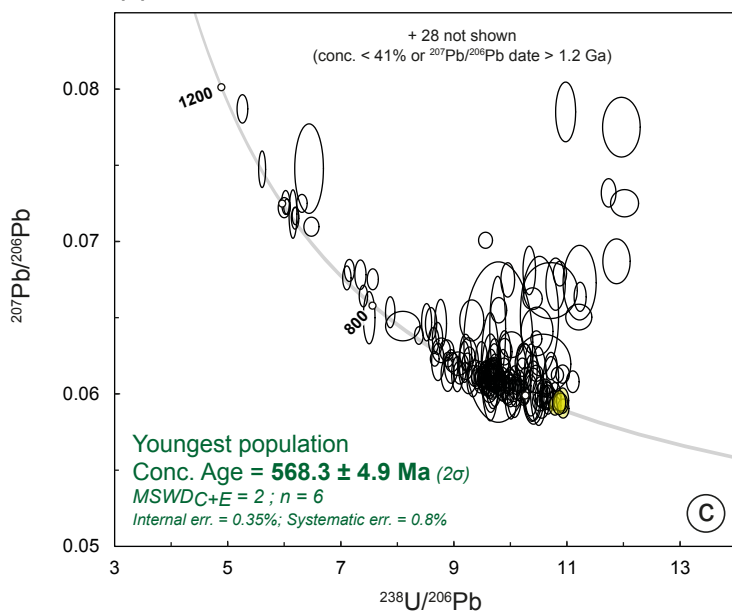
(a) PIL-16-01 Pilat metasandstone



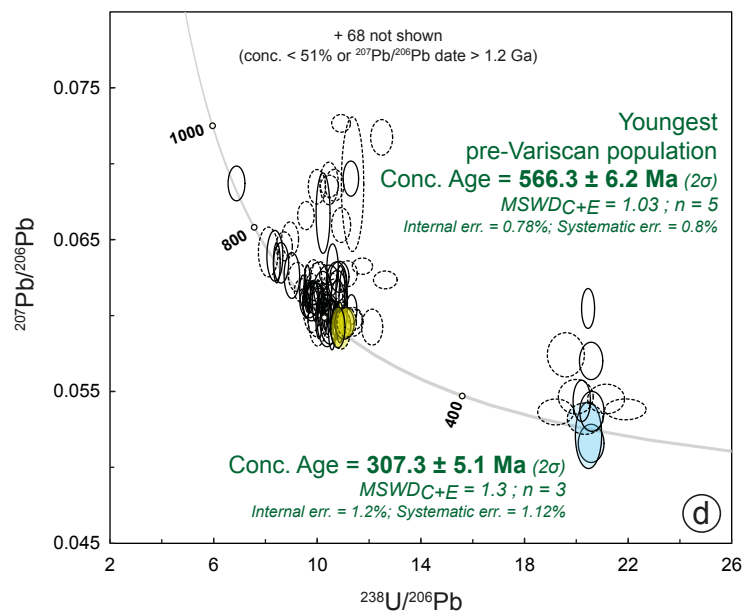
(b) SEN-16-01 Senouire metasandstone



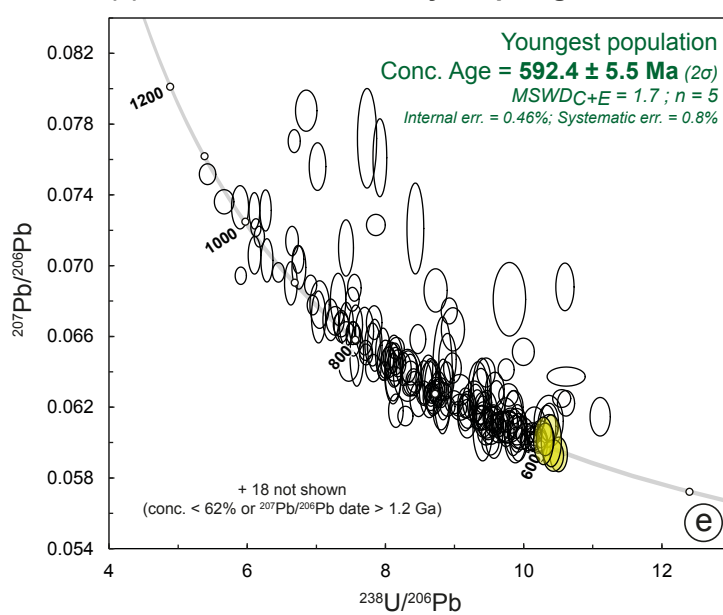
(c) CHA-16-02 Cévennes meta-arkose



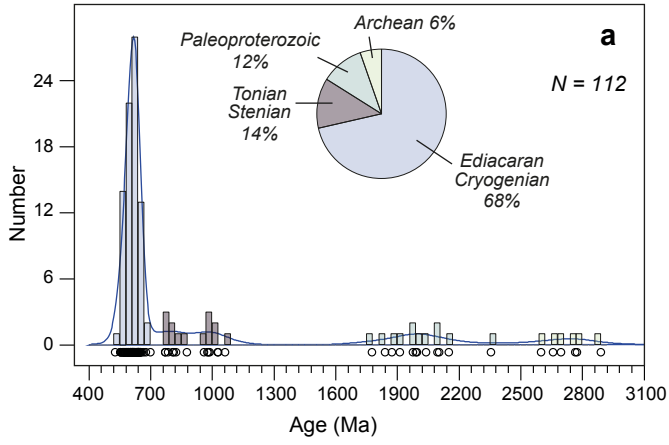
(d) TN46 Tournon paragneiss



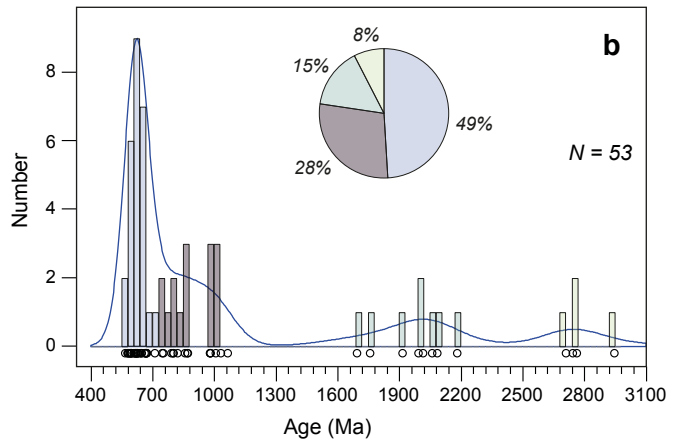
(e) PdB-16-01 Pont-de-Bayzan paragneiss



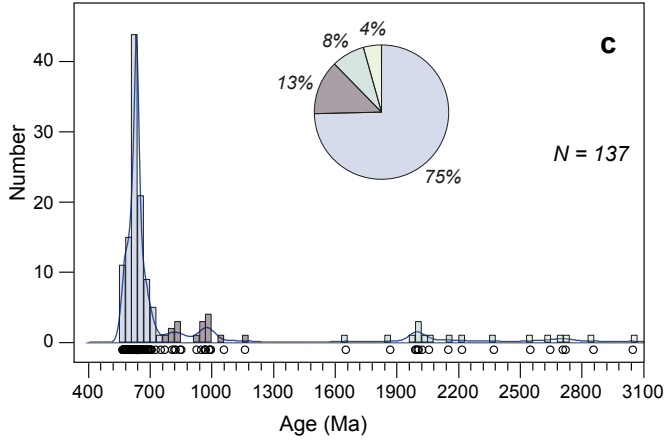
PIL-16-01 Pilat metasandstone



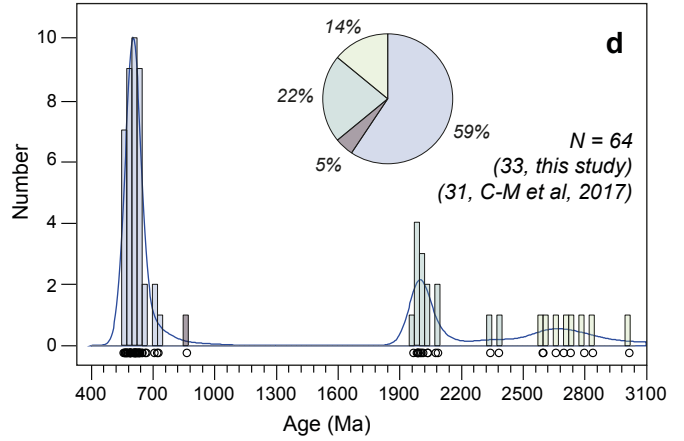
SEN-16-01 Senouire metasandstone



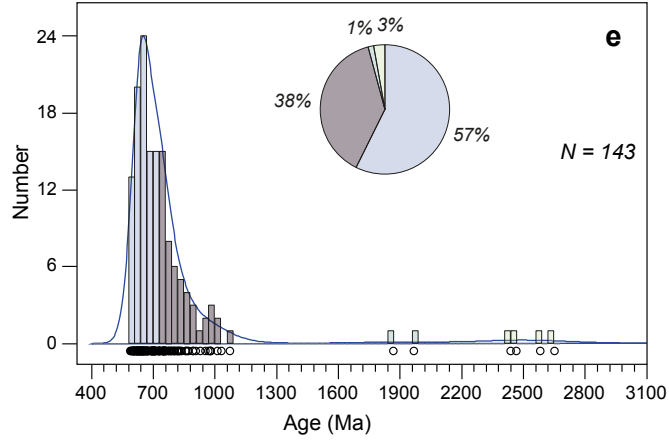
CHA-16-02 Cévennes meta-arkose

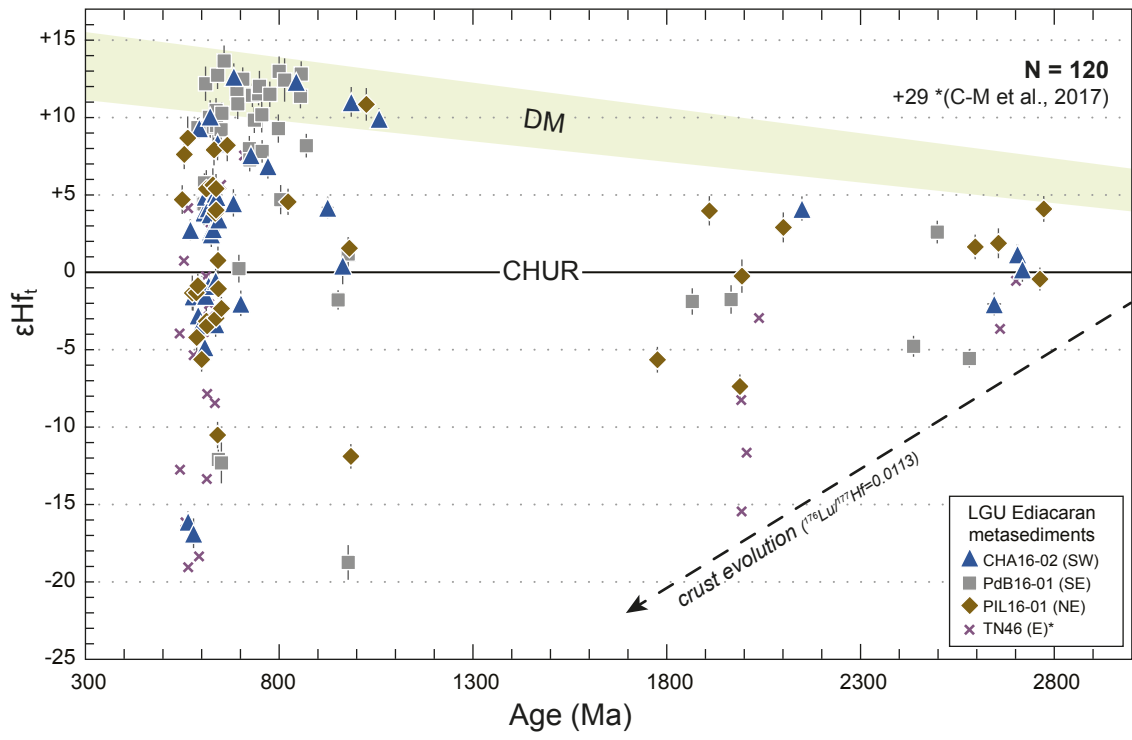


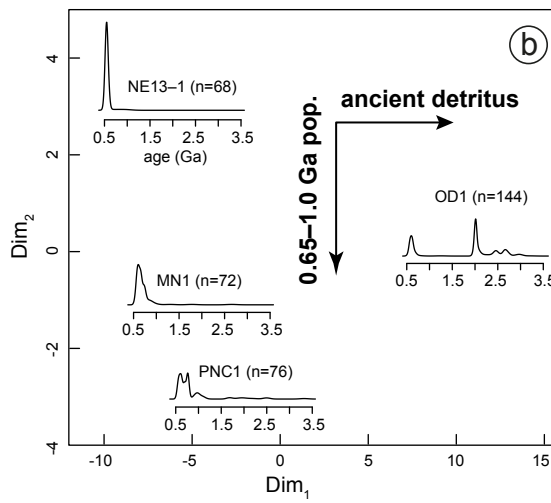
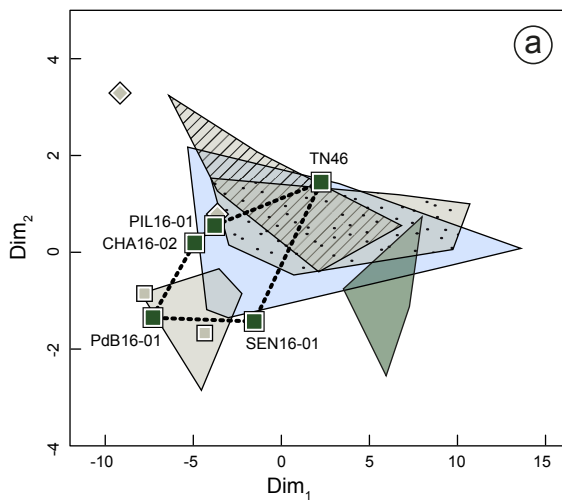
TN-46 Tournon paragneiss



PdB-16-01 Pont-de-Bayzan paragneiss





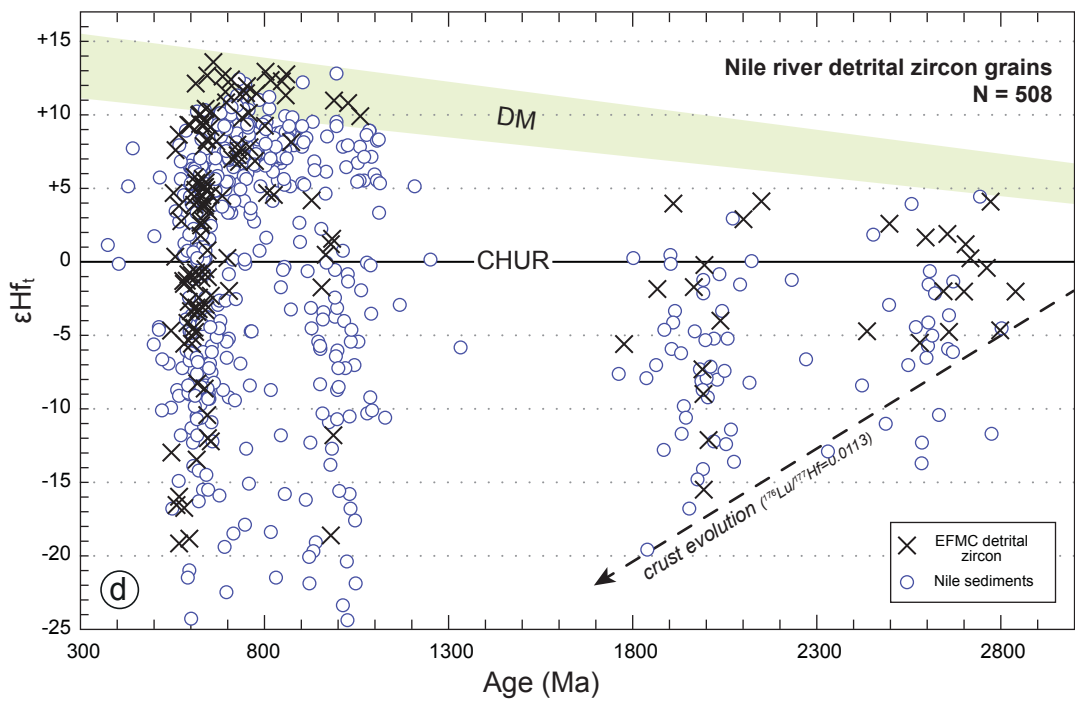
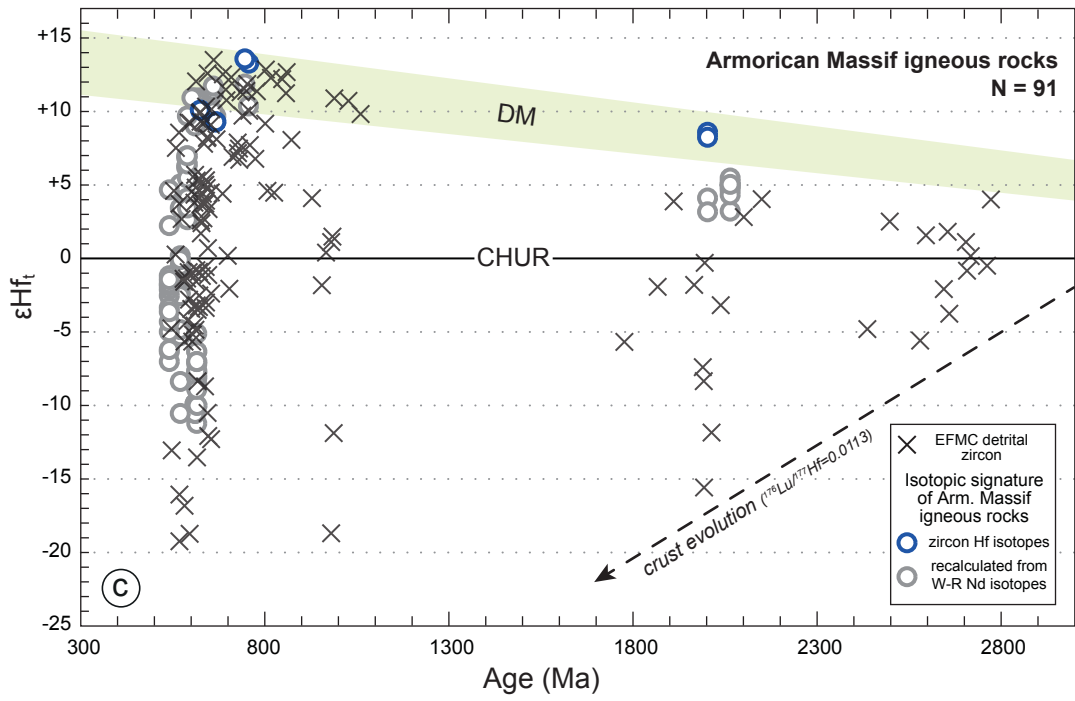
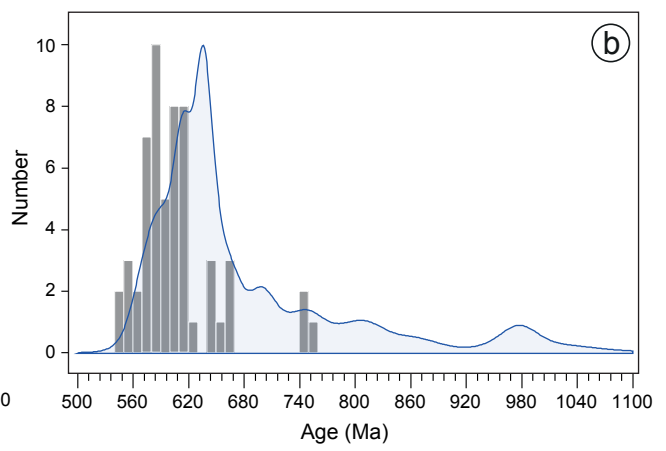
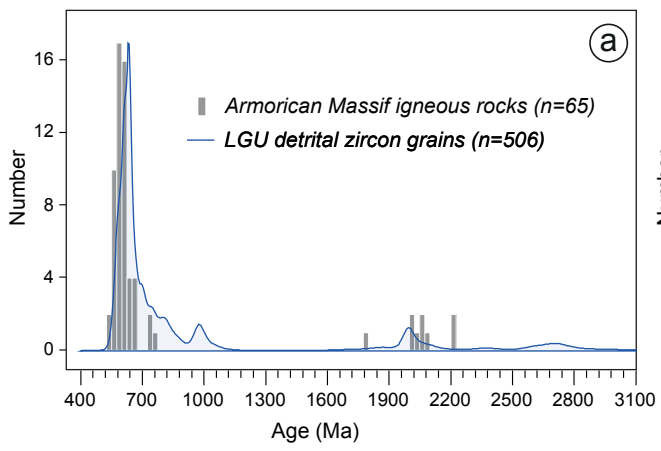


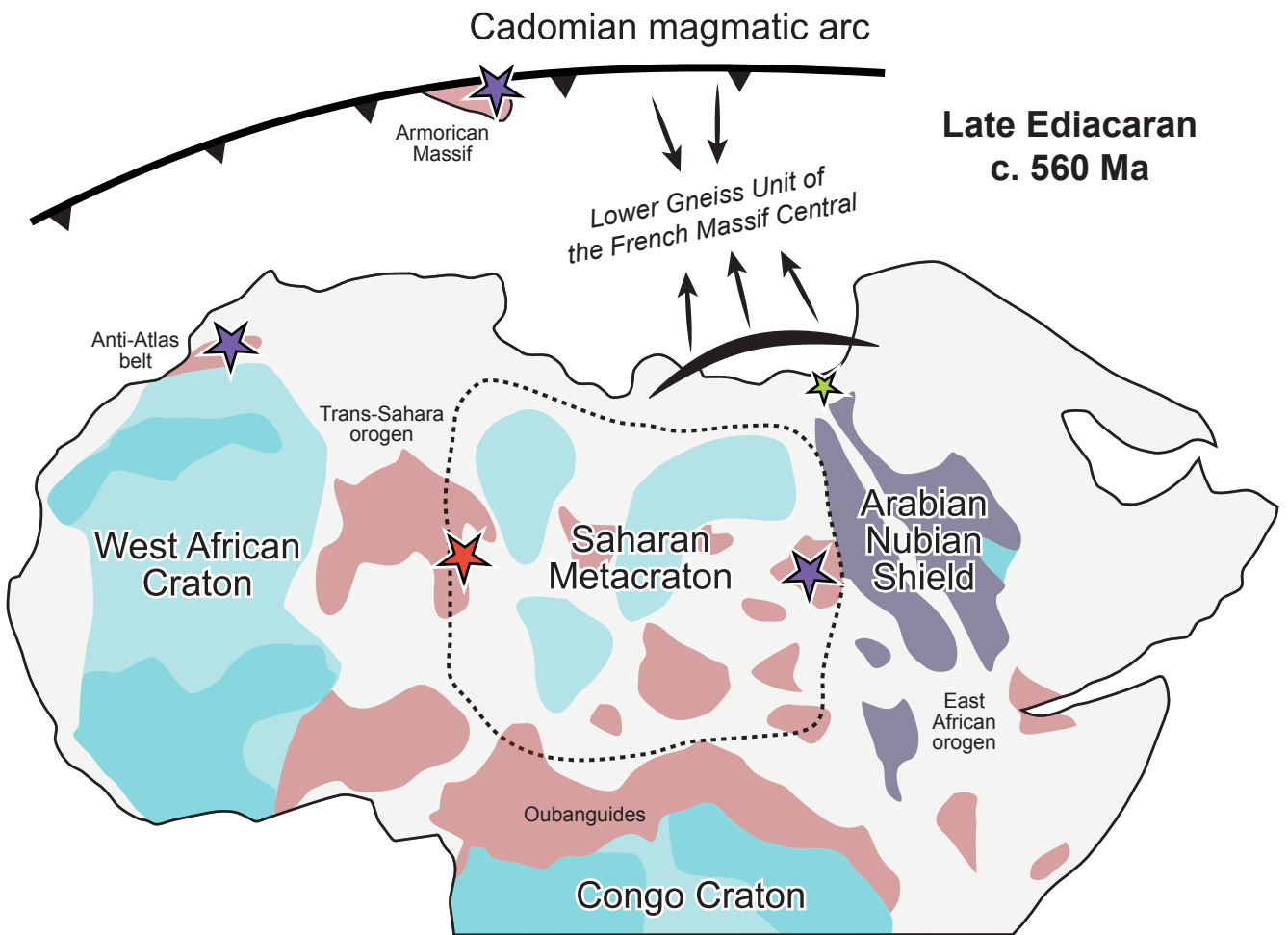
High-grade metasediments

- Galicia-Trás-os-Montes (n=5)
- Lower Gneiss Unit (Eastern Massif Central)

(Very) Low- to medium-grade (meta)sediments

- Central Iberian/West Asturian-Leonese (n=10, 1 excluded)
- Saxo-Thuringian (n=16)
- Teplá-Barrandian (n=6)
- Cantabrian (n=6)
- Montagne Noire (Southern Massif Central)
- Armorican Massif





**Panafrican
orogens**

- Ediacaran – late Cryogenian crust with supra to subchondritic Nd-Hf signatures
- Ediacaran – late Tonian crust with strictly suprachondritic Nd-Hf signatures
- early Cryogenian – Tonian crust with suprachondritic Nd signatures
- early Cryogenian – Tonian crust with subchondritic Nd signatures
- Stenian crust
- Paleoproterozoic to Archean crust (exposed/covered craton)

